Cross Talk in Full-Field Optical Coherence Tomography

Boris Karamata, Marcel Leutenegger, and Theo Lasser
Laboratoire d'Optique Biomédicale, École Polytechnique Fédérale de Lausanne, 1015 Lausanne, Switzerland
boris.karamata@a3.epfl.ch

The formation of cross-sectional images of biological tissues requires the discrimination between light conveying useful information—that is, propagating directly from object to image—from the abundant parasitic light caused by multiple scattering inherent to turbid media [1, 2]. In optical coherence tomography (OCT[a]) [3], selective detection of light undergoing a single backscatter event (reflection imaging) and rejection of multiply scattered light (MSL) has been successfully achieved by combining temporal coherence gating and confocal spatial filtering [4, 5].

[a]OCT systems incorporating sample objectives with relatively a large numerical aperture (NA) so as to provide enhanced en face optical sectioning are quite arbitrarily designated optical coherence microscopy (OCM) systems. Since our investigation and conclusions are independent of the NA, we use the term "OCT" throughout this chapter.

Handbook of Full-Field Optical Coherence Microscopy: Technology and Applications
Edited by Arnaud Dubois

ISBN 978-981-4669-16-0 (Hardcover), 978-981-4669-17-7 (eBook)
www.panstanford.com

In full-field OCT[b] (FF-OCT) [8–10], the rejection of MSL is even more challenging due to the large illumination field and the loss of confocal spatial filtering in a parallel detection scheme [1, 11]. As our investigation will reveal, despite temporal gating detection capabilities can be severely limited by cross talk, an unwanted signal contribution caused by MSL from the full-field illumination volume [11].

In this chapter, we develop a model accounting for multiple scattering in OCT and use it to predict cross talk effects in FF-OCT. As will be shown both theoretically and experimentally, the amount of cross talk strongly depends on the sample properties and system parameters and, above all, on the nature of the illumination. When the latter is spatially coherent, as obtained, for example, with a broadband laser, the cross talk contribution is generally a serious limitation to the method [11]. At the other extreme, spatially incoherent illumination (SII), as provided, for example, with a thermal light source, prevents the cross talk contribution [12].

Given this decisive advantage of SII, it would be interesting to understand the initial motivations for developing FF-OCT systems based on either type of illumination. In the early nineties, soon after the first developments of point-scanning OCT systems, two major development tasks were recognized: to improve the resolution and to increase the measurement speed. Image resolution at cellular level would secure sounder diagnosis and offer new applications in developmental biology [13], while faster measurement would allow the elimination of artefacts due to sample motions as well as observation of dynamic phenomena [14, 15].

On one side, FF-OCT systems with SII were primarily developed to obtain a very good resolution at minimum complexity and cost [8, 16, 17]. En face imaging inherent to FF-OCT allows the exploitation of thermal light sources, while maintaining a high enough signal-to-noise ratio (SNR) provided measurement time is sufficiently long. Since the naturally broad spectrum of thermal light sources yields very high longitudinal resolutions [18, 19], they are a valuable alternative to the sophisticated femtosecond

[b]With FF-OCT we implicitly consider full-field illumination. FF-OCT measurements for en face or three-dimensional imaging can also be performed with point-scanning [6] or line-scanning systems [7].

lasers used in point-scanning OCT, whose cost and complexity can be restrictive. Moreover, en face imaging is the configuration of choice with respect to transverse resolution [6, 8]. Surprisingly, a key advantage of the method—the cross talk rejection properties offered by thermal light sources—was not emphasized by most researchers with the exception of Fercher et al. [19]. However, as discussed further below, the weakness of FF-OCT systems relying on SII is first due to the low modal power of thermal light sources [19–21], and then to measurement speed limitations imposed by the insufficient performance of conventional detectors. This technological shortage, which obviously also affects FF-OCT with SCI, is even more important in this other method given its purpose explained hereafter.

On the other side, FF-OCT systems relying on spatially coherent illumination (SCI) were developed with the main aim to increase the measurement speed thanks to parallel acquisition [10, 22–24]. The idea was to exploit the broadband spatially coherent light sources developed for point-scanning OCT, that is, mainly superluminescent diodes (SLDs) and short-pulsed lasers. At that time, given the lack of appropriate quantitative knowledge, cross talk was mainly considered as a potential limitation to the method. The primary concern, when aiming at high measurement speed, was the technological barrier set by the too low readout speed and dynamic range of two-dimensional detectors such as CCDs[c] [9, 15]. Indeed, to ensure a high enough SNR, while avoiding saturation of the detector due to the large reference signal component, it is necessary to average a relatively large collection of images at the same position [16, 18]. Moreover, the reconstruction of the interferometric OCT signal requires high sampling in the longitudinal dimension, which further increases the amount of images to be generated [16, 18]. Thus the image acquisition speed is limited by the time required for the accumulation of many images and the detector readout time. Thus requirement for high image acquisition rate–ultimately limited by the capabilities of the analog-to-digital converter,[c] considerably slows down the FF-OCT

[c]For a two-dimensional sensor such as CCDs, readout speed is determined by the capabilities of the analog-to-digital converter typically allowing for an acquisition speed of hundred frames per second, while the dynamic range available for signal capture is determined by the full well depth capacity of a pixel, which is typically

method. To address this crucial technological issue, the flexibility of design in CMOS detectors was exploited to develop arrays with a custom integrated circuit around each pixel performing the following operations: 1) high-pass filtering cancelling out the large reference signal, 2) amplification and rectification of the heterodyne signal, and, 3) low-pass filtering. The implementation of this parallel heterodyne detection scheme provides a higher dynamic range and requires a lower sampling rate to obtain the envelope of the OCT signal. Very high image acquisition rates were demonstrated with a prototype of such detectors [9, 22]. Presently, this can also be achieved with a commercially available custom camera (Heliotis AG) endowed with the same functionality and more pixels [25, 26].

Moreover, high-speed measurement with sufficient sensitivity for OCT biological imaging requires a spatially incoherent light source brighter than the commonly used thermal light sources, whose modal power is inherently low [19–21]. A few ways for creating such an ultrabright extended light source are briefly discussed in the conclusion of this chapter.

A new generation of FF-OCT systems incorporating an ultrabright spatially incoherent light source and a custom detector array may well compete with ultrafast Fourier domain OCT (FD-OCT) systems [14, 27] in terms of image acquisition speed. A parallel operation in the Fourier domain, which requires line illumination and a two-dimensional detector, provides longitudinal cross-sectional images without mechanical scanning [7]. Tremendous acquisition speeds without compromising on SNR and the number of pixels can be attained thanks to a more efficient use of light for building OCT signals yielding sensitivity superior to that of time domain OCT [27]. This remarkable feature allows the use of CCD detectors with good SNR while avoiding saturation by the large reference signal component. With potentially comparable acquisition speeds for en face cross-sectional images, the new generation of FF-OCT systems might become a valuable alternative to FD-OCT for fast three-

limited to a few hundred thousands photo-electrons. The corresponding dynamic range (without cooling system)—given by the square root of this number of photo-electrons, is then only of two orders of magnitude.

dimensional measurements, as briefly discussed in the conclusion of this chapter.

In Section 4.1 we will define cross talk noise in FF-OCT and provide a deeper analysis of its coherence properties. From there we will first derive the key assumptions on which an OCT model accounting for multiple scattering should be built, and second explain how cross talk can be suppressed. Our model is presented in Section 4.2 and the results of experimental validation are reported in Sections 4.3 and 4.4. In Section 4.4 we investigate the role of important sample properties and of the key system design parameters in relation to cross talk-generated noise for FF-OCT with SCI. The interest of this comprehensive study is twofold. First, it allows testing the validity of our theoretical model, which rests on assumptions fundamentally different from those on which other existing models are based; and, second, it offers a method to determine the quantitative contribution of cross talk in FF-OCT relying on SCI. In Section 4.5 we will present experiments that reveal how SII enables FF-OCT imaging free of cross talk noise. Finally, we will discuss our theoretical and experimental investigation and draw general conclusions. In particular, we will discuss the more complex models based on the extended Huygens–Fresnel principle [28], which rest on assumptions fundamentally different from ours.

Our study provides a deeper understanding of the role played by multiple scattering in coherence based detection methods and allows to better evaluate limitations in FF-OCT.

4.1 Optical Cross Talk in FF-OCT

In full-field optical coherence tomography (FF-OCT), the abundant amount of multiply scattered light (MSL) generates optical cross talk between the parallel detections channels. Despite temporal coherence gating, a fraction of such cross talk light usually generates a coherent cross talk noise contribution to the OCT signals. In Sections 4.1.1 and 4.1.2 we define more precisely cross talk noise. We analyze the coherence properties of cross talk light and determine the degree of correlation with the OCT reference signal,

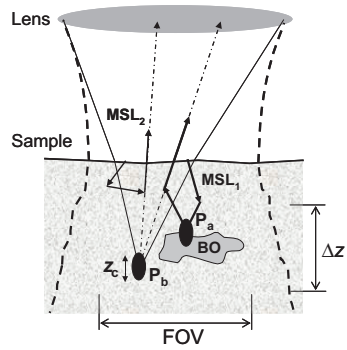

Figure 4.1 Scheme of an interferometer arm with a diffuse sample showing different optical paths yielding cross talk in FF-OCT: full-field illumination beam (dashed lines), field of view (FOV), ideal probe volume (P_b), virtual probe volume (P_a), backscattering object (BO), longitudinal scan range (Δz), longitudinal resolution (z_c), forward multiply scattered light from BO (MSL_1), and MSL from the scattering medium alone (MSL_2).

that is, its propensity to generate a detectable noise. In Section 4.1.3 we explain how cross talk-generated noise can be suppressed by exploiting the spatial coherence properties of the OCT light source.

4.1.1 *Origin and Definition of Cross Talk Noise*

To define more precisely cross talk-generated noise that can occur in typical FF-OCT interferometers operated in the time domain (see Section 4.3.1), we will consider Fig. 4.1, which schematically represents the interferometer sample arm with several multiple scattering trajectories within the sample. The latter consists of a backscattering object (BO) embedded in a homogeneous scattering medium.

The full-field illumination beam diffusing through the sample determines the overall scattering volume. The ideal measurement volume is determined by the field of view (FOV) of the optical system and by the range (Δz) of the scan depth. The resolution of a given OCT system defines the size of a probe volume (P_n). With an appropriate design, the tranverse resolution and the depth resolution are determined by the numerical aperture (NA) of

the sample arm objective and by the source coherence length l_c, respectively. A probe volume has a longitudinal dimension $z_c = l_c/2n$, where n is the sample refractive index. For each probing depth, a collection of probe volumes are defined in the same transverse plane (perpendicular to the optical axis). Each of these probe volumes P_n is imaged on a specific portion of the detector array (group of pixels), designated detector C_n.

Ideally, for a depth z, defined by the reference mirror position, only light originating from a given probe volume P_n should be detected by its conjugated detector C_n. Consider the two probe volumes P_a and P_b conjugated to the detectors C_a and C_b, respectively (see Fig. 4.1). Propagation of MSL across the whole scattering volume biases the ideal one to one correspondence between a given probe volume and its conjugated detector. The cross talk-generated noise on a detector can be defined as the total coherent signal contributions brought by light originating from all probe volumes in the measurement volume, with the exception of the probe volume conjugated to the detector at a given depth z. A coherent contribution may occur only if the random paths taken by MSL are equally long (within the distance of correlation determined by the source autocorrelation function g_0) to the ideal ballistic paths set by the reference mirror position. Figure 4.1 illustrates how forward MSL originating from the probe volume P_a (MSL_1), or from the homogeneous scattering medium (MSL_2), can reach the detector C_b conjugated to probe volume P_b, while taking identical path lengths.

4.1.2 *Qualitative Analysis of the Cross Talk Contribution*

We propose to examine under what circumstances cross talk light—which necessarily consists of MSL—can interfere with the reference field (see Fig. 4.2). In other words, we need to determine the degree of correlation between MSL and the reference field in OCT.

In a typical FF-OCT setup with a spatially coherent light source, such as illustrated in Fig. 4.2, the reference field consists of a planar wavefront (RW) at the two-dimensional detector array, whereas the light scattered by a diffuse sample produces a distorted random wavefront (SW). The degree of correlation

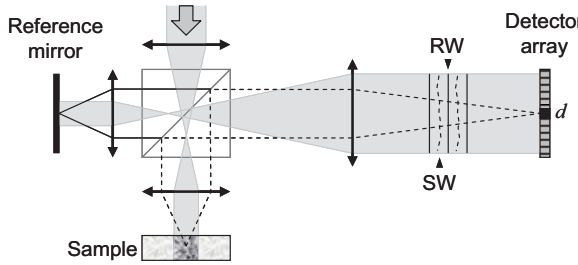

Figure 4.2 Scheme of an interferometer showing the distorted wavefronts from the sample (SW) and the plane wavefronts from the reference mirror (RW). The speckle size, corresponding to the Airy disc size *d*, is shown at the detector array.

between these two interfering fields depends both on their spatial and temporal coherence properties. It seems to be widely accepted that the interference process at the detector results from complex phenomena difficult to model. The analysis presented here below reveals that this is actually not the case.

4.1.2.1 Spatial coherence of cross talk light

With SCI the reference field is obviously spatially coherent. Let us examine the spatial coherence properties of the sample field. With a spatially coherent light source and a diffuse sample, the light backscattered from the sample generates a speckle pattern on the detector array. The distorted wavefront corresponding to this pattern interferes with the reference field producing a speckle pattern whose intensity obeys a known statistical distribution [29, 30]. More importantly the speckle size roughly corresponds to the Airy disc size *d* as determined by the objective NA of the detector arm (see Fig. 4.2). By definition, phase difference across the Airy disc is negligible. In an appropriate design, the pixel size of the detector array should be no more than half the size of the Airy disc so as to fulfil Shannon's condition for optimal spatial sampling. This means that, independent of the random orientation of the wavefront reaching the detector array (RW), the phase difference is negligible across a single pixel detector, which is exactly the condition for

spatial coherence [31]. Thus, any portion of the distorted wavefront viewed by a single pixel detector can be but spatially coherent.[d]

Therefore, we can conclude that, in an FF-OCT design with adequate spatial sampling, despite distortion of the backscattered sample field due to multiple scattering, the portion of light collected by a single detector is spatially coherent. This means that any potential reduction of correlation between the reference and sample fields cannot be attributed to a loss of spatial coherence in the sample field.

4.1.2.2 Interference with multiply scattered light

Conservation of spatial coherence of light detected from the sample arm by a single detector is a necessary but not a sufficient condition to ensure the correlation between the reference and the sample field.

As explained in Section 4.1.1, at a given probing depth set by the reference mirror position, with MSL, equivalent optical path lengths can exist in the sample arm for different scattering paths outside of the ideal conjugated probe volume to be imaged. Obviously, if the random path lengths exceed the distance of correlation determined by the source autocorrelation function g_0, no interference can occur. Now, the following question becomes crucial: can the correlation be degraded by the random scattering events with MSL for path lengths falling within the coherence length set by g_0? Should this be the case, a reduction of correlation can be caused only by a temporal stochastic process such as Brownian motion generating a random phase relationship between the sample and reference fields. Actually, although a totally motionless biological sample is seldom met in practice, this assumption is generally valid in the context of OCT detection. In this case, a sample can be considered as locally motionless provided that fluctuations of the interference fringes obtained with the sample and reference fields are negligible during the measurement time interval necessary for recording one fringe period. This condition is fulfilled as shown in another

[d]Numerous studies on the degree of spatial coherence implicitly deal with areas much larger than the speckle size. For instance, for a large sampling area, Yang et al. showed how the loss of spatial coherence of forward-scattered light propagating in a turbid medium is related to the number of scattering events [32].

both theoretical and experimental study of the unfavorable case of an aqueous suspension of microspheres where the interference fringes are shown to be fully stationary (frozen) during the relevant measurement time in OCT [33].

Thus, contrary to a widespread belief, it turns out that, despite the random scattering events along various paths taken by MSL, the latter remains correlated to the reference field when falling within the source coherence length, exactly like for ballistic light. Under these conditions, the degree of correlation depends only on the source autocorrelation function g_0. It follows that MSL can strongly contribute to the OCT signal in the form of a coherent noise, which cannot be discriminated from the useful OCT signal (ballistic light) despite temporal coherence gating. This unwanted signal contribution exhibits strong speckle fluctuations as soon as the random phase delays of MSL—caused by a spatial stochastic process—fall within the range of the source's central wavelength. Agreement between theory and measurements regarding the statistical distribution of the speckle intensity strongly supports the view that MSL interference with the reference signal can be maximal ($g_0 = 1$) [33].

We conclude that MSL is fully correlated to the reference field for equivalent optical path lengths in both interferometer arms. The average magnitude of OCT signals at a given position depends only on the amount of light—ballistic or multiply scattered—taking an optical path equivalent to the one in the reference arm as set by the mirror position. Multiple scattering is responsible for a coherent noise contribution in the form of a speckled component, but not for a loss of correlation between the reference and sample fields.

4.1.2.3 Questions raised by our analyses

The above analyses provide a qualitative insight into cross talk-generated noise and raise two important questions:

(1) How important is the cross talk noise contribution relative to the useful OCT signal?
(2) How can cross talk noise be suppressed?

To answer the first question we present in Section 4.2 an OCT model which accounts for MSL and allows quantifying the cross

talk noise contribution as a function of various relevant physical parameters. Regarding the second question, we will explain in the next section how cross talk-generated noise can be drastically reduced by exploiting the spatial coherence properties of the light source.

The above analyses also raise questions relative to OCT models built on assumptions incompatible with our findings. Indeed, sophisticated models based on the extended-Huygens principle and the use of mutual coherent functions (MCFs) rest on both spatial and temporal statistical averaging [34, 35]. Thus, they inherently assume a large sampling area when calculating the MCFs, as well as a long enough measurement time per probe volume, which would lead to some statistical averaging inducing a decorrelation between the reference and sample fields. The reduced degree of correlation obtained with such complex calculations leads to the prediction of lower cross talk noise contributions. Interested readers can find a more thorough discussion of this topic in Ref. [33].

4.1.3 *Cross Talk Noise Suppression with Spatial Coherence Gating*

Generally, with full-field illumination large amounts of MSL are generated and collected (cross talk light). Therefore, cross talk-generated noise can be suppressed only by preventing the interference between MSL and the reference field. As explained hereafter, this can be achieved thanks to a low degree of spatial coherence within the full-field as generated by a spatially incoherent light source. The idea is to create, for each parallel detection channel, an effect equivalent to confocal spatial filtering by exploiting spatial coherence effects. This will provide a "spatial coherence gating" which one can figure out in a relatively straightforward and intuitive manner.

The principle of spatial coherence gating relies on the creation of mutually incoherent probe volumes within the sample. The probe volumes occupy adjacent positions with center coordinates $x_S y_S$ in the sample transverse cross section. In the interferometer, such probe volumes are duplicated in the reference arm at twin positions $x_R y_R$ on the reference mirror. When a reference field

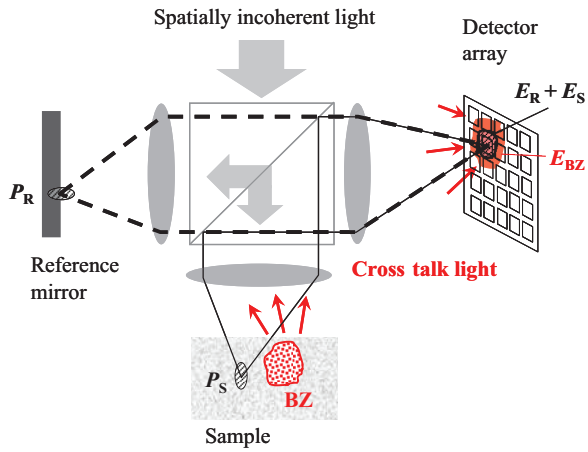

Figure 4.3 Schematic illustration of the spatial coherence gating concept. With spatially incoherent illumination, light from the probe volume P_S can interfere only with light from its replica P_R. Cross talk light from the backscattering zone (BZ) produces a field that does not contribute to the OCT interference signal.

(E_R) and a sample field (E_S) recombine on the detector plane, interference can occur only if images of the corresponding twin probe volumes P_R and P_S are superimposed as illustrated in Fig. 4.3. The reference field, which is not perturbed by scattering, acts as a spatial coherence gate allowing interference only with light originating from the corresponding sample probe volume.

Assume cross talk noise generated by the sample backscattering zone (BZ) reaching the detector on which E_R and E_S overlap (see Fig. 4.3). An additional field contribution E_{BZ} due to cross talk is created on this detector yielding a total field $E_T(x, y) = E_R(x_R, y_R) + E_S(x_S, y_S) + E_{BZ}(x_{BZ}, y_{BZ})$. Since, by design, $E_{BZ}(x_{BZ}, y_{BZ})$ does not share the same spatial coherence properties as $E_R(x_R, y_R)$, interference cannot occur and the last term $E_{BZ}(x_{BZ}, y_{BZ}) = 0$. This selective interference allows cross talk noise suppression in full-field illumination.

Optimal cross talk noise rejection, that is, an amount of coherent noise owing to MSL as low as in point-scanning OCT, is obtained provided there is a good overlap between probe and coherence

volumes $V_c = l_c \ A_c$, as defined by L. Mandel and E. Wolf [36]. Therefore, coherence volumes matching the probe volumes should be created. Generally, the longitudinal dimension of both coherence and probe volumes is the same in OCT since both are determined by the source coherence length l_c. Therefore, it suffices to match the cross-sectional area of a probe volume A_p with the coherence area A_c of the coherence volume. Since the Airy disc and coherence area share the same physical properties, namely, phase fluctuations significantly lower than 2π [31], the critical condition $A_p \approx A_c$ is quite naturally met in a practical case, given that the same sample arm is used both for illumination and detection. Thus, achieving an efficient spatial coherence gating requires only the pupil of the sample arm to be filled with spatially incoherent light. This is generally the case in a conventional optical setup used for OCT, where a spatially incoherent light source is imaged onto the sample [8, 12]. Some mathematical insights into the equivalence $A_p \approx A_c$, as well as more formal design guidelines for optimal coherence gating and power throughput can be found in Refs. [12, 20].

We would like to point out that spatial coherence gating in a parallel detection scheme offers even more than an effect equivalent to confocal spatial filtering for each channel. Indeed, besides rejection of MSL, spatial coherence gating yields an enhanced longitudinal and tranverse resolution identical to that of confocal imaging systems. This extremely interesting property, obtained whenever an extended source is combined with an interferometric detection process, was described by several authors in various contexts (Davidson et al. [37], Lee et al. [38], and more recently by Somekh et al. [39]). In a closely related context, Sun and Leith showed the equivalence of extended-source image plane holography and the confocal imaging process [40].

4.2 Theory and Model

A comprehensive model of OCT requires modeling both the light propagation in random media and the interference process, which depends on coherence properties of the sample field. Light propagation in random media, including temporal aspects, can

be described quite successfully by the time-resolved diffusion theory [41, 42]. However, this theory is based on the diffusion approximation, which becomes valid only after a few scattering events [43] yielding delays of a few picoseconds [42, 44]. Such delays, which largely exceed typical source coherence times in OCT, correspond to considerable path lengths, that is, in the order of one millimeter. Therefore, models based on the diffusion approximation fail to properly describe MSL distribution in the range of interest met in OCT where relevant path lengths can also be one to three orders of magnitude lower. A calculation performed by a Monte Carlo simulation can provide the spatiotemporal distribution of light within the entire range of interest [42, 44]. Several existing models of OCT are based on Monte Carlo simulation, for example [45–47]. However, in principle, the latter cannot account for the coherence properties of MSL, whose knowledge is indispensable in the context of coherent detection techniques.

Here, we present a comprehensive model of OCT accounting for multiple scattering. The model rests on the two important assumptions derived in Section 4.1:

(i) The portion of the backscattered sample field collected by the detector (by each detector if there is more than one like in FF-OCT) is spatially coherent (see Section 4.1.2.1)
(ii) The interference fringes signal is stationary (frozen) during the time for recording one fringe period (see Section 4.1.2.2).

4.2.1 *Mathematical Description*

The mathematical description of interfering fields in an amplitude-splitting interferometer where both ballistic light backscattered once and MSL are collected in the sample arm (see Fig. 4.4), is greatly simplified with the above two assumptions. Indeed, assumption (i) implies that the phase of the electrical field is constant across the detector area. Thus, the description of the interference process does not require cross-correlation functions across the detector plane, leaving only its perpendicular dimension z to be considered in the model. Assumption (ii) allows a description of the interference process with a sample field altered by spatial

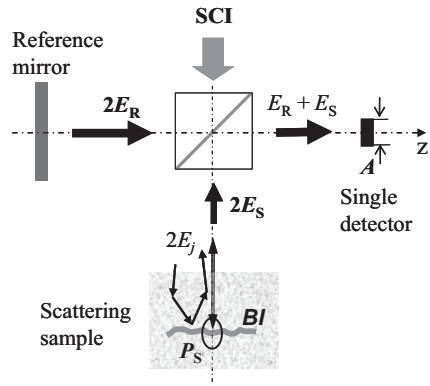

Figure 4.4 Scheme of an amplitude splitting interferometer with broadband spatially coherent illumination (SCI). E_R and E_S are the reference and sample fields, respectively. E_j are components of E_S corresponding to ballistic light backscattered once from backscattering interface *BI* (double line) and MSL (single line). Interference between E_R and E_S is considered on a single detector A—whose size is smaller than the Airy disc—located at a conjugated distance with the sample probe volume P_S. The beam splitter equally divides light. The full optical setup is shown in Fig. 4.5.

stochastic processes constant over the time for building one fringe period. Thus, calculation of the cross-correlation function between the sample and reference fields requires only accounting for spatial stochastic processes brought by the sample, but not for temporal stochastic processes.

Let us first calculate the intensity for a sample consisting of a simple plane mirror. Consider a broadband source power spectrum $I(k)$ where $k = 2\pi/\lambda$ is the wavenumber. Assuming 100% reflectivity of the reference mirror and a reflectivity $r(k)$ for the sample mirror, the electrical fields E_R and E_S reflected from the reference and from the sample arm, respectively, can be expressed for a given wavenumber as

$$E_R = \mathrm{Re}\left\{\sqrt{I(k)}\exp\left(i(kz - \omega t)\right)\right\} \tag{4.1}$$

$$E_S = \mathrm{Re}\left\{r(k)\sqrt{I(k)}\exp\left(i(\varphi(k) - \omega t)\right)\right\}, \tag{4.2}$$

where z is the reference mirror position and $\phi(k)$ a phase argument depending on the position of the sample mirror.

When the waves recombine in the interferometer, the total resulting intensity as a function of the wavenumber is

$$\begin{aligned} I_{\mathrm{T}}(k) &= \left\langle |E_{\mathrm{R}}(k) + E_{\mathrm{S}}(k)|^2 \right\rangle \\ &= I(k)\left[1 + r^2(k) + 2r(k)\mathrm{Re}\left\{\exp\left(i(\varphi(k) - kz)\right)\right\}\right], \end{aligned} \tag{4.3}$$

where the brackets denote averaging over a time interval much longer than the time of an optical cycle.

The total intensity on the detector is obtained by integrating over the whole spectrum.

$$\begin{aligned} I_{\mathrm{T}} = \int_0^\infty I_{\mathrm{T}}(k)\mathrm{d}k = \int_0^\infty I(k)\left(1 + r^2(k)\right)\mathrm{d}k \\ + 2\mathrm{Re}\left\{\int_0^\infty I(k)r(k)\exp\left(i\varphi(k)\right)\exp\left(-ikz\right)\mathrm{d}k\right\}. \end{aligned} \tag{4.4}$$

The first term, independent of z, is a constant intensity I_0, while the second one corresponds to the Fourier transform of the power spectrum weighted by the sample spectral reflectivity. Therefore, Eq. 4.4 is equivalent to

$$I_{\mathrm{T}} = I_0 + 2\mathrm{Re}\left\{\mathbb{F}\left[I(k)r(k)\exp\left(i\varphi(k)\right)\right]\right\}. \tag{4.5}$$

Let us now consider the more general case met in OCT where both ballistic light backscattered once and MSL contributions are present. Here, the sample field E_{S} is the sum of many contributions $E_j = \mathrm{Re}\{u_j(k)\ \exp(ikL_j)\}$, each corresponding to a light ray having undergone a random path owing to interactions with the scattering medium. The length L_j is the additional geometrical path length accumulated by a multiply scattered photon (double path), relative to ballistic photons, and $u_j(k)$ is a field-weighting coefficient proportional to the field magnitude. The total sample field is

$$E_{\mathrm{S}}(k) = \mathrm{Re}\left\{\sum_{j=1}^{N} E_j(k)\right\} = \mathrm{Re}\left\{\sqrt{I(k)}\sum_{j=1}^{N} u_j(k)\exp\left(i(kL_j - \omega t)\right)\right\}. \tag{4.6}$$

Repeating for a scattering sample the calculation's steps that led to Eq. 4.5, and assuming the coefficients $u_j(k)$ to be independent

of the wavelength (i.e., either no, or constant absorption over the spectrum), we obtain

$$I_T = I_0 + 2\mathrm{Re}\left\{\mathbb{F}\left[I(k)\sum_{j=1}^{N} u_j \exp\left(ikL_j\right)\right]\right\} \tag{4.7}$$

and by virtue of the convolution theorem

$$I_T = I_0 + 2\mathrm{Re}\left\{\mathbb{F}\left[I(k)\right] \otimes \sum_{j=1}^{N} u_j \mathbb{F}\left[\exp\left(ikL_j\right)\right]\right\}. \tag{4.8}$$

According to the Wiener–Khinchin theorem $\mathbb{F}[I(k)]$ is the source autocorrelation function $g(z)$. Defining $I'(\Delta k) = I(k)$, where $\Delta k = k - k_0$, and $\lambda_0 = 2\pi/k_0$ is the central wavelength of the light source, $g(z)$ can be expressed as follows

$$g(z) = \mathrm{F}\left[I(k)\right] = \mathbb{F}\left[I'(\Delta k)\right] = \exp\left(ik_0 z\right)\mathbb{F}\left[I'(k)\right] = \exp\left(ik_0 z\right) g_0(z), \tag{4.9}$$

where $g_0(z)$ is a complex function whose argument and amplitude vary slowly relative to $g(z)$ and whose module is the envelope of $g(z)$. The second Fourier transform in Eq. 4.8 corresponds to a delta function.

$$\mathbb{F}\left[\exp\left(ikL_j\right)\right] = \delta(z - L_j) \tag{4.10}$$

After substitution of Eqs. 4.9 and 4.10 into Eq. 4.8, one obtains

$$I_T = I_0 + 2\mathrm{Re}\left\{\sum_{j=1}^{N} g_0(z)\exp\left(ik_0 z\right) \otimes u_j \delta(z - L_j)\right\}. \tag{4.11}$$

This expression reveals that the nature of the signal consists of a convolution of the autocorrelation function with randomly distributed delta functions, located at random L_j positions. Exploiting the shift properties of the delta function, we can simplify Eq. 4.11 by

$$I_T = I_0 + 2\mathrm{Re}\left\{\exp\left(ik_0 z\right)\sum_{j=1}^{N} u_j g_0(z - L_j)\exp\left(-ik_0 L_j\right)\right\}. \tag{4.12}$$

This equation provides the intensity detected as a function of the reference mirror position z. In OCT that relies on heterodyne detection, the reference mirror is scanned at constant velocity inducing a modulation of the signal at the Doppler frequency. The effective OCT

signal is the electrical current i_D obtained after bandpass filtering at the Doppler frequency and subsequent envelope demodulation. The first signal processing operation suppresses the constant term I_0 and the second operation removes the carrier modulation $\exp(ik_0z)$ and leaves a signal proportional to the module of the filtered signal. Such signal processing yields the following detected current:

$$i_D(z) \propto \left| \sum_{j=1}^{N} u_j g_0(z - L_j) \exp\left(-ik_0 L_j\right) \right|. \tag{4.13}$$

This equation reveals that, despite multiple scattering, all the light detected in OCT interferes coherently within the coherence length around a position z imposed by the reference mirror. Moreover, for each position z, the sum of factors with random arguments leads to speckle formation, which accounts for the randomness of the measured signals.

4.2.2 *Calculation of the Mean Signal*

Since we are interested in determining the mean contribution of multiple scattering in OCT, we will calculate the mean of the random signal detected. The summation in expression (4.13) corresponds to a sum of random phasors, different around each position z, which results in a single random phasor with amplitude $A(z)$ and phase $\Phi(z)$. Assuming the argument of $g_0(z)$ to vary slowly relative to $\exp(-ik_0 L_j)$, one can write

$$\begin{aligned} &\sum_{j=1}^{N} u_j g_0(z - L_j) \exp\left(-ik_0 L_j\right) \approx \sum_{j=1}^{N} u_j \left| g_0(z - L_j) \right| \exp\left(-ik_0 L_j\right) \\ &= \sum_{j=1}^{N} \alpha_j(z) \exp\left(-i\theta_j\right) = A(z) \exp\left(i\Phi(z)\right). \end{aligned} \tag{4.14}$$

Classical results from statistical optics derived by Goodman can now be exploited. His calculations of the statistical distribution of a sum of random phasors for various cases rest on two important initial assumptions [31]:

(i) The phases θ_j are uniformly distributed over the interval $[0,2\pi]$.

(ii) The amplitude α_j and phase θ_j of the jth elementary phasor are statistically independent of each other, as well as of the amplitudes and phases of all elementary phasors.

Because we have $L_{\max} >> 2\pi/k_0$ in all experiments and because we can assume the paths L_j to be randomly distributed in the interval [0, $L_{\max}$], the phase argument $\theta_j = k_0 L_j$ is uniformly distributed between 0 and 2π, as required by the first assumption.

The second assumption implies that both $g_0(z)$ and u_j are independent of L_j. In the first approximation, the independence between $g_0(z)$ and L_j is verified if the module of $g_0(z)$ varies slowly with L_j relative to the function $\exp(-ik_0 L_j)$. This condition is met for $\Delta\lambda << 1/k_0$, which is usually the case in OCT. However, u_j and L_j are generally interdependent. Fortunately, as shown in Appendix A, it is sufficient to verify independence locally, that is, for a relatively short path length interval ΔL in the order of the source coherence length l_c. Such local independence is generally achieved in OCT, as in our further experiments, and we can therefore assert the second assumption.

Therefore, the results derived by Goodman can be directly applied to the general case of OCT in which both ballistic light backscattered once and MSL contributions are present. The random phasor sum described by Eq. 4.14 obeys a probability density function, whose mean and variance are [31]

$$\overline{A(z)} = \sqrt{\frac{\pi}{2}}\sigma(z) \tag{4.15}$$

and

$$\sigma^2(z) = \frac{\overline{\alpha_j^2(z)}}{2}, \tag{4.16}$$

respectively. $\overline{A(z)}$ is directly proportional to the mean value of $i_D(z)$ in Eq. 4.13, i.e., to the mean amplitude of the random OCT signal. Such mean signal can be roughly measured by averaging demodulated signals as explained in Section 4.3.1. Applying Eq. 4.16 to the random phasor sum described by Eq. 4.14 yields

$$\sigma^2(z) = \frac{1}{2}\overline{u_j^2 \left|g_0(z - L_j)\right|^2} = \frac{1}{2N}\sum_{j=1}^{N} U_j \left(g_0(z - L_j)\right)^2, \tag{4.17}$$

leading to

$$\sigma(z) = \sqrt{\frac{1}{2N} U_j \otimes g_0^2(z)}, \tag{4.18}$$

where $U_j = (u_j)^2$ is the intensity coefficient corresponding to light traveling a path length L_j.

$\overline{A(z)}$ is directly proportional to the mean value of $i_D(z)$ in Eq. 4.13, that is, to the mean amplitude of the random OCT signal. Such mean signal can be roughly measured by averaging demodulated signals as explained in Section 4.3.1.

Thus the mean signal detected in OCT can be calculated by combining Eqs. 4.15 and 4.18. However, to perform this calculation, one still needs to know the coefficients U_j, which are proportional to the intensity $I_S(L_j)$ measured in the sample at depth $L_j/2$ from the sample mirror. $I_S(L_j)$ corresponds to the spatiotemporal distribution of the intensity, that is, of photons. The calculation of such a distribution lends itself very well to a Monte Carlo simulation [42, 44]. Therefore, our model combined with a Monte Carlo simulation, allows one to calculate OCT signals in accounting for ballistic (backscattered once) and MSL. The important features of the Monte Carlo simulation further used in our model are described in Section 4.3.4.

Our model was developed for a backscattering interface covered with scattering medium. This corresponds to most practical cases of interest such as biological interfaces, generally made of densely packed scatterers [48]. Even ballistic light backscattered once by these complex submicrometric structures reaches the detector with random phase delays and gives rise to speckle formation. The samples used in all further experiments are made of a mirror covered with a scattering solution. In this case, all ballistic light is reflected by a mirror and reaches the detector with the same phase argument. Thus, the sample field distribution actually corresponds to a deterministic phasor plus a random phasor sum, instead of a purely random phasor sum. The term “deterministic phasor” signifies here that the phasor’s argument is not randomized owing to multiple scattering. It is important to thoroughly treat this case in order to be able to reliably model the samples used in our experiments. The calculations for this case, provided in Appendix B, yield a slightly more complex solution, whose implementation is less straightforward.

4.2.3 *Integration of Monte Carlo Results*

Practical integration of Monte Carlo simulation's results into our model requires the following analysis. A Monte Carlo simulation provides a photon distribution whose density is proportional to the mean intensity I_v in a vth sampling volume determined by the detector size and temporal distribution ($\Delta t \propto \Delta L$ range). The resolution determines an average path of length L_v of all path lengths L_j falling into the vth sampling volume. To express Eq. 4.18 as a function of I_v, the sum operation is distributed into V sampling volumes, each containing m_{v+1}–m_v of the N elements. This yields

$$\begin{aligned}\sigma^2(z) &= \frac{1}{2N}\sum_{j=1}^{N} U_j \left(g_0(z-L_j)\right)^2 \\ &= \frac{1}{2}\sum_{v=1}^{V}\frac{1}{m_{v+1}-m_v}\sum_{j=m_v+1}^{m_{v+1}} U_j \left(g_0(z-L_j)\right)^2 \\ &= \frac{1}{2}\sum_{v=1}^{V} I_v \left(g_0(z-L_v)\right)^2 \end{aligned} \tag{4.19}$$

leading to

$$\sigma(z) = \sqrt{\tfrac{1}{2} I_v \otimes g_0^2(z)} \tag{4.20}$$

and

$$\overline{A(z)} = \sqrt{\frac{\pi}{2}}\sigma(z) = \sqrt{\frac{\pi}{4} I_v \otimes g_0^2(z)}. \tag{4.21}$$

Practical implementation details for the calculation of I_v are provided in Section 4.3.4.

4.3 Method for Cross Talk Investigation

In this section we describe the setup (Section 4.3.1) and the samples (Section 4.3.2) used for the measurement of cross talk in FF-OCT with SCI. Explanations on the presentation of our experimental results and simulation details are provided in Sections 4.3.3 and 4.3.4, respectively.

4.3.1 *Setup*

The experimental setup used for FF-OCT is illustrated in Fig. 4.5. A broadband spatially coherent light source, coupled to a single mode fiber, is launching light into a free space Michelson interferometer. Light is equally divided by a nonpolarizing beam splitter into the reference and the sample arm containing identical microscope objectives with a $\times$ 10 magnification (L_3 and L_3') and a numerical aperture (NA) of 0.25. Lenses L_1, L_2 and L_3 are positioned so as to obtain a collimated beam illuminating the sample with a 420 μm Gaussian intensity profile measured at full-width at half-maximum (FWHM). The sample is imaged with a $\times$ 30 magnification by lenses L_3 and L_4, which form a microscope as illustrated in the sample arm in Fig. 4.5.

The source is an SLD. Its spectrum, centered on 810 nm with 17 nm bandwidth at FWHM, corresponds to a coherence length (l_c) of 34 μm at FWHM. The SLD (Superlum 381-HP2) delivers a power of around 1 mW onto the sample.

Interference between light backscattered from the sample and the reference mirror (RM) can occur only when the optical path length difference lies within the source coherence length. The

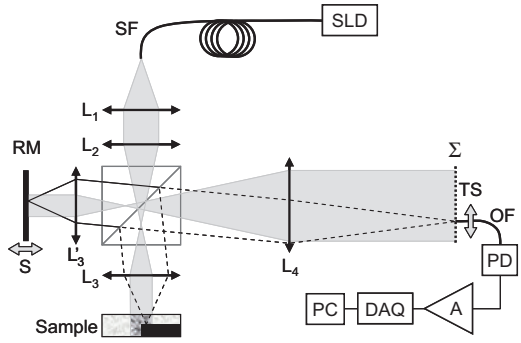

Figure 4.5 Scheme of an FF-OCT setup. Superluminescent diode (SLD); single-mode fiber (SF); reference mirror (RM); voice coil scanner (S); achromatic lenses (L_1, L_2, and L_4); microscope objective $\times$ 10, NA = 0.25 (L_3 and L_3'); translation stage (TS); 50 μm core optical fiber (OF); photodiode (PD); preamplifier (A); data acquisition card (DAQ); personal computer (PC).

reference mirror is mounted on a voice coil scanner (S) and scanned longitudinally at constant velocity over a depth of 750 μm at a frequency of 2 Hz with a 90% duty cycle. The resulting 6.7 kHz Doppler frequency modulation permits heterodyne detection.

To dispose of large dynamical range, avoid potential electronic cross talk and gain flexibility, a single movable detector is used instead of a detector array. The detection is made with a single photodiode (PD) to which light is delivered by an optical fiber (OF) moved in 120 μm steps across the image plane Σ with a motorized translation stage (TS). Each step corresponds to 4 μm on the sample side, a distance larger than the microscope objective resolution, which is around 2 μm. Such spatial undersampling allows for a larger measurement range while maintaining a reasonably low acquisition time. Note, however, that the 50 μm core of the optical fiber roughly matches the resolution of the microscope objective, which is around 60 μm after magnification with L_4.

The photocurrent produced by the photodiode is amplified and high-pass filtered by a low noise pre-amplifier (A). The signal is then digitized with a 12 bit analog-to-digital converter on a data acquisition card (DAQ) and numerically processed in a personal computer (PC). With the SLD, the signal processing consists of 0.6 kHz band-pass filtering around the 6.7 kHz Doppler frequency with a second-order Chebyshev filter, followed by envelope reconstruction with the Hilbert transform. The DAQ is triggered by the voice coil scanner at each new depth scan. An experimental sensitivity of −75 dB is obtained with the SLD when 25 demodulated signals are averaged.

Samples consisting of scattering solutions, such as used in our studies (see Section 4.3.2), undergo Brownian motion, that is, the scatterers are randomly changing their positions and inducing time-varying signals. Thus, a different random signal, modulated by speckle noise, is obtained for each OCT measurement. Taking the average of the envelopes a few OCT signals measured sequentially allows reducing speckle noise. Thanks to this operation—possible owing to the dynamic nature of our samples—one can easily obtain OCT measurements representative of the average cross talk signals, which is the value of interest in our study. Relevant speckle statistics and temporal behavior are thoroughly investigated in Ref. [33]. For instance, averaging 25 and 50 demodulated signals as in our

further experiments, reduces the speckle contrast by 80% and 85%, respectively.

Some experiments require comparison with a confocal system, as used in point scanning OCT, without need for tranverse scanning. A confocal configuration with properties equivalent to point-scanning OCT can be obtained by simply removing lens L_2. The monomode fiber is then imaged onto the sample, providing a confocal spot illumination. The confocal configuration leads to an experimental sensitivity of -96 dB when 25 demodulated signals are averaged.

4.3.2 *Sample*

The sample consists of a cleaved GaAs edge coated with gold and embedded in a scattering solution maintained in a cell. The latter is limited by a 150 μm thick cover glass on the objective side. The distance Δz between the reflecting edge and the cover glass can be accurately varied. The scattering solution consists of monodisperse polystyrene microspheres in de-ionized water. Ultrasound shaking is applied for distributing the microspheres homogeneously. Tests revealed that, despite sedimentation, the sample optical properties remain stable during at least 10 minutes.

The absorption being negligible at the wavelengths used, the solution can be considered as purely scattering. Independent of the type of solution used (size of microspheres), the concentration is adjusted separately to a scattering coefficient $\mu_S = 6.2\ \text{mm}^{-1}$ using the collimated transmission method given in Ref. [49]. The cell inner thickness Δz determines the number of scattering mean free paths, that is, the sample optical density (OD) defined as $2\Delta z\mu_S$ when accounting for double optical path. The source wavelength ($\lambda \cong 810$ nm in air), as well as the size and refractive index ($n = 1.59$) of the microspheres suspended in water, yield an anisotropy parameter g defined as the average cosine of the scattering angles, that can be calculated with the Mie theory [50]. We use three different sizes of microspheres, that is, anisotropies g, in our experiments (see Section 4.4.1).

Depending on the experiment, the sample is moved in the transversally so as to present in the detection plane Σ either a full-mirror interface or half a mirror with the cleaved edge positioned on

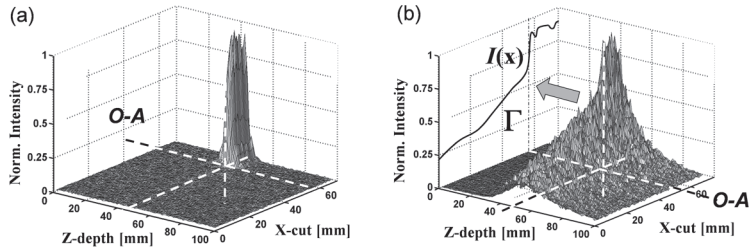

Figure 4.6 Cross-sectional FF-OCT image of a cleaved mirror with the edge break on the optical axis ($O - A$): (a) in water; (b) in scattering solution (8 OD, $g = 0.93$); $I(x)$: projection of the maximum intensity profile in the plane Γ.

the optical axis. In this contribution, these positions are designated "full-mirror sample" and "half-mirror sample," respectively.

4.3.3 *Presentation of Experimental Results*

The graphical representation of the experimental results presented further in this chapter is not trivial and requires detailed explanations.

Consider the measurement performed with the FF-OCT system and the half-mirror sample, as described in the previous two sections. The three-dimensional plots shown in Fig. 4.6 are the cross-sectional images of the half-mirror sample—with the normalized intensity represented along the vertical axis—obtained in water and in a scattering solution, respectively. The plots correspond to the average cross talk signal obtained from a few tens of demodulated signals acquired at different time intervals. As explained in Section 4.3.1, random time-varying signals are obtained due to speckle fluctuations caused by the Brownian motion of the scatterers. In water, the half-mirror interface is clearly resolved in both dimensions, whereas with the scattering solution the cross talk spreads into the whole sample, degrading both the longitudinal and the tranverse resolution. Practically, a quantitative comparison between theory and experiment in a three-dimensional representation is difficult. Therefore, cross talk effects are investigated independently for the tranverse and the

longitudinal dimensions with the half- and the full-mirror samples, respectively.

The tranverse cross talk extent is represented by the maximum intensity profile $I(x)$ corresponding to a projection of the three-dimensional intensity plot along the optical axis (O–A) onto plane Γ, as shown in Fig. 4.6b. The edge break is always located on the optical axis. To reduce image acquisition time, we use measurements that cover 325 μm, from which 75 μm are on the cleaved mirror side and 250 μm are on the other side. $I(x)$ plots are obtained by averaging 25 demodulated signals so as to reduce the speckle contrast by 80% (see Section 4.3.1). To allow comparison with the ideal case of full cross talk rejection, we illustrate in all graphs the corresponding projection of the cleaved edge intensity profile measured in water.

The extent of longitudinal cross talk is measured along the optical axis with the full-mirror sample. The plots are normalized and shown as a function of the reference mirror displacement. The longitudinal plots correspond to the average of 50 demodulated signals yielding 85% lower speckle contrast (see Section 4.3.1). To allow comparison with the ideal case of full cross talk rejection, we illustrate the envelope of the autocorrelation function in all graphs.

Measurements are represented with corresponding theoretical results obtained with our model. Comparison of theoretical and experimental results for the tranverse dimension is less straightforward than for the longitudinal dimension, where all curves are normalized. Normalizing to the maximum intensity would not be reliable since the signals measured on the cleaved mirror side are very noisy (see results in Section 4.4) owing to rippled illumination profile, coating damage, and possibly microsphere aggregates sticking to the surface of the mirror. Therefore, experimental data are adjusted with a multiplicative factor K_f so as to obtain a least-square-fit difference with the theoretical curves. The adjustment is performed on data measured on the opposite side of the cleaved mirror.

On the practical side, between each measurement with a new parameter (see Section 4.4), we cleaned the sample cell with ethylene. Before introducing the scattering solution, we filled the sample cell with water to allow an accurate mirror positioning into focus.

4.3.4 *Monte Carlo Simulation Details*

The Monte Carlo simulation, which accounts for the sample properties and optical parameters, provides the spatiotemporal distribution of light collected from the sample arm. The algorithm used in our Monte Carlo simulation is described elsewhere, for example, by Wang et al. [51]. We used a Mie scattering distribution for unpolarized light at each particle interaction [50]. In our practical case we ignored it because absorption is negligible for polystyrene microsphere.

The position and the angle of a photon at the sample interface (after crossing the sample), determine on which detector it will fall. According to the rules of geometrical optics, photons collected by a detector originate from a sampling area whose points are conjugate to the detector area. For a scattering sample, the position and size of the detector actually determine a sampling area from which photons virtually originate. The accumulated path length delay (L_j) of a photon defines its position along the depth axis. The sampling volume introduced in Section 4.2.3 is then determined by the dimensions of the sampling area and by the longitudinal sampling resolution, which amounts to 1 μm in our simulation. The sampling area, which corresponds to the tranverse resolution of our system, is 4 μm.

For our specific case (mirror embedded in scattering solution), the intensity distribution $I_v(L_j)$, proportional to the number of photons m_v in a sampling volume v, is treated as follows. First, the ballistic component (interaction with the mirror only), here responsible for the major part of the high peak located at L_0 (sample mirror position), is removed from the distribution so that $\sigma(z)$ can be calculated from Eq. 4.22 in Appendix B. The mean OCT signal can then be derived from Eqs. 4.23–4.25 in Appendix B. More details of such calculation are shown for a case study in Ref. [33]. Note that, for the more general case involving backscattering interface with random microstructures (unlike mirror), the treatment is far more straightforward, since Eq. 4.21 can be directly applied to $I_v(L_j)$.

Particular care must be taken to implement the correct physical scaling factors into the simulations. Since L_j represents the geometrical path length, the corresponding length scale was multiplied

by the water refractive index ($n = 1.33$) and divided by two, so as to account for the optical path length and reference mirror displacement, respectively. In addition, the width of g_0 must be divided by n.

4.4 Experimental and Theoretical Results for Cross Talk Noise

In this section we will investigate how cross talk signals are correlated to the main properties of the sample, namely the optical density (OD) and the anisotropy (g) of the scattering solution (Section 4.4.1). The cross talk signals are measured with the setup described in Section 4.3.1. For each parameter, theoretical and experimental results are plotted on the same graph. In another experiment presented in Section 4.4.2, the intensity of the cross talk signal relative to that of the useful OCT signal (ballistic light) will be investigated as a function of the probing depth. At the end of this section, relevant additional results are briefly mentioned before the conclusions (Section 4.4.3).

4.4.1 *Dependence on Sample Properties*

Cross talk noise dependence on the anisotropy of the scattering solution is investigated first. Results with three different anisotropy parameters are shown in Fig. 4.7a and Fig. 4.7b for the full-mirror sample and for the half-mirror sample, respectively (see Section 4.3.2). Microsphere diameters smaller ($d = 350$ nm), roughly equal ($d = 750$ nm) and larger ($d = 2050$ nm) than the illumination wavelength ($\lambda = 810$ nm in air, that is, 610 nm in water) were used, yielding the anisotropy parameters $g = 0.55$, $g = 0.85$, and $g = 0.93$, respectively [50]. For the three solutions the scattering coefficients were adjusted to $\mu_S = 6.2$ mm^{-1} as explained in Section 4.3.2, leading to OD $= 8$ for $\Delta z = 650$ μm. Note that the chosen anisotropy coefficients are representative of biological tissues, typically lying between 0.7 and 0.99 [52].

Let us first comment on the results obtained with the full-mirror sample. A wide-angle scattering solution is obtained with

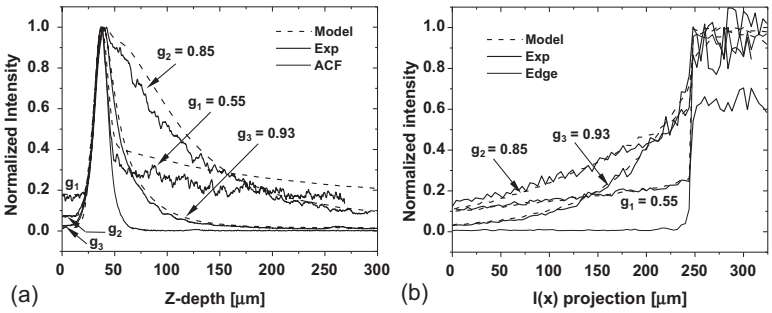

Figure 4.7 Experimental (Exp) and theoretical (Model) results obtained in FF-OCT for various anisotropies (g) with OD $= 8$, $D = 420$ μm, and NA $= 0.25$: (a) correlogram envelopes for the full-mirror sample, and envelope of the source autocorrelation function (ACF) given for reference; (b) projections of maximum intensity profiles obtained with the half-mirror sample, and the corresponding profile in water given for reference (Edge).

$g = 0.55$, resulting in a nearly flat cross talk signal extending over a long distance, while a large peak emerges at the mirror interface. This peak, whose width corresponds to the envelope of the source autocorrelation function (ACF), is caused by the ballistic light reflected by the mirror. The contrast, rather than the longitudinal resolution, is reduced. With anisotropy $g = 0.85$ moderate forward scattering is obtained giving rise to a long tail dramatically reducing the longitudinal resolution. With anisotropy $g = 0.93$ relatively high forward scattering is obtained resulting in limited MSL delays and in a signal width around 50% broader than the ACF envelope at FWHM.

With the half-mirror sample, cross talk effects are more pronounced with $g = 0.93$ showing that the moderately delayed MSL spreads quite significantly into the tranverse dimension. This study tends to show that, in our experimental conditions, the most deleterious cross talk effects, in terms of large noise contribution spreading far from the ideal probe volume, are obtained for microsphere diameters approaching the source central wavelength. In principle, for a larger NA, more wide-angle scattered light is collected and the worst cross talk figure is obtained for smaller microsphere diameters. Our model allows precisely determining the ratios λ/d yielding the best or the worse figure for each specific case.

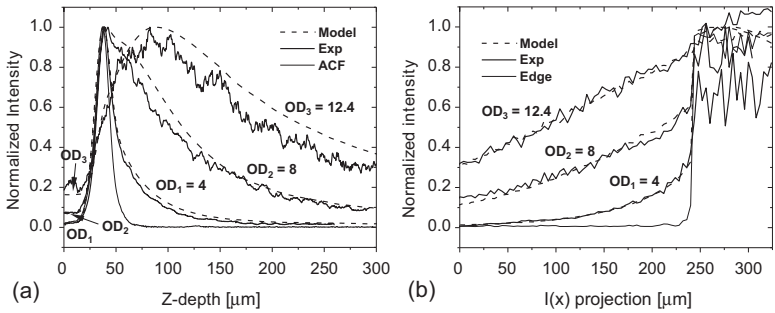

Figure 4.8 Experimental (Exp) and theoretical (Model) results obtained in FF-OCT for various optical densities (ODs) with $\mu_S = 6.2$ mm^{-1}, $g = 0.85$, $D = 420$ μm, and NA = 0.25: (a) correlogram envelopes for the full-mirror sample, and envelope of the source autocorrelation function (ACF) given for reference; (b) projections of maximum intensity profiles obtained with the half-mirror sample, and the corresponding profile in water given for reference (Edge).

Cross talk noise dependence on the sample optical density (OD) is investigated here below. The cross talk signals measured for three different ODs with $g = 0.85$ are shown in Fig. 4.8a and Fig. 4.8b for the full- and the half-mirror sample, respectively. The different OD values are obtained by varying the cell thickness Δz while maintaining the mirror edge in focus, as explained in Section 4.3.2. With a constant $\mu_S = 6.2$ mm^{-1}, the thicknesses $\Delta z = 320$ μm, $\Delta z = 650$, and $\Delta z = 1000$ correspond to OD = 4, OD = 8, and OD = 12.4, respectively. As expected, the measurements clearly show that the smaller the OD of the sample, the less cross talk is generated, and the better is the resolution. With the thickest sample, the peak signal is well behind the mirror interface showing the dominant role played by delayed MSL relative to ballistic light.

The corresponding theoretical results obtained with the model presented in Section 4.2 are in very good agreement with experimental data for nearly all cases investigated. However, as can be observed with the full-mirror sample, the model systematically leads to slightly higher amplitudes for cross talk signals relative to the intensity peak. This means that the MSL contribution is slightly overestimated. One possible explanation for this small systematic difference could be the omission of polarization effects

in our theoretical model that could lead to overestimation of the multiply scattered component relative to the ballistic component. This hypothesis is supported by the results obtained when varying the anisotropy of the scattering solution (see Fig. 4.7a) where the systematic difference is the highest for the lowest microsphere diameter (i.e., highest anisotropy) and vice and versa. Indeed, according to Mie theory, polarization effects increase inversely with the microsphere diameter. The interested reader can find a more comprehensive discussion on minor discrepancies between our theoretical and experimental results [11].

4.4.2 *Cross Talk Contribution Relative to the Useful Signal*

The above presented results reveal how major sample properties affect the cross talk noise and, in turn, the longitudinal and tranverse resolution. However, the normalization procedure used for the presentation of the results is hiding an important consequence of cross talk. Indeed, in FF-OCT, the significant MSL contribution causes a signal enhancement highly dependent on the sample properties.

To gain more insight into the contribution of MSL responsible for cross talk-generated noise relative to the ballistic light component (useful signal), we will investigate the signal attenuation in the sample as a function of the probing depth and compare it to the ideal single-backscattering model used in point-scanning OCT [53]. In this model, which accounts for ballistic light only (backscattered once), the amplitude follows a negative exponential decrease according to Lambert–Beer's law. The significant MSL contribution in FF-OCT causes a signal enhancement that is highly dependent on the sample properties. The deviation from Beer's law caused by the MSL contribution is investigated in the experiment described here below.

The full-mirror sample was used with a scattering solution adjusted to $\mu_S = 6.2\ \text{mm}^{-1}$, first for a relative forward scattering solution ($g = 0.93$). We varied the OD by increasing the sample thickness (Δz) in regular steps while maintaining the reflecting interface in focus, according to the procedure described in Section 4.3.3. The signal was measured for each thickness in both full-field and confocal configurations (see Section 4.3.1). The exponential intensity decrease, proportional to $\exp(-\alpha \Delta z)$ predicted by Beer's

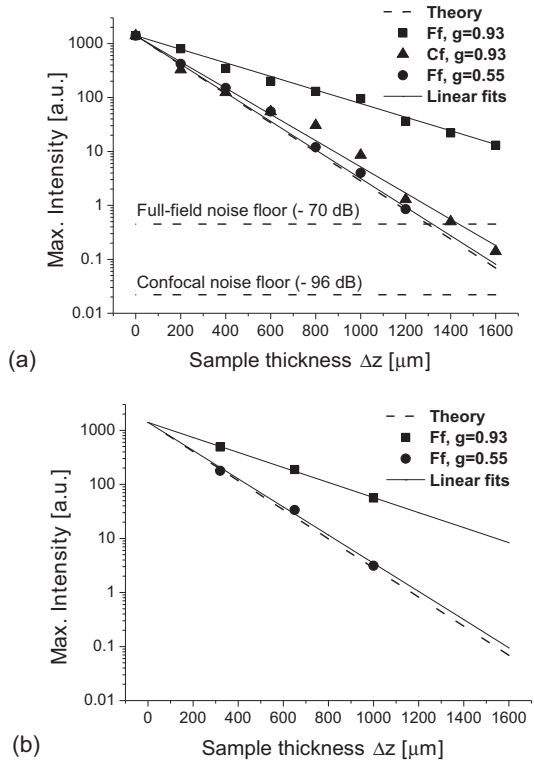

Figure 4.9 Maximum intensities of OCT signals obtained with the full-mirror sample for $\mu_S = 6.2$ mm^{-1} versus sample thickness for different anisotropies (g) and configurations. The decrease in intensity, for full-field configuration (Ff) with $D = 420$ μm, NA = 0.25, and confocal configuration (Cf) with NA = 0.25, is compared with the exponential decrease predicted by Lambert–Beer's law (Theory). Linear fits are illustrated for all cases. (a) Experimental results. (b) Theoretical results obtained with our model.

law ($\alpha = \mu_S = 6.2$ mm^{-1}), is plotted in Fig. 4.9. This figure shows as well the noise floors attained with the interferometer in the full-field configuration (sensitivity of -75 dB) and in the confocal configuration (sensitivity of -96 dB). The optical depth of our standard condition (OD = 8) corresponds to $\Delta z = 650$ μm.

With the full-field configuration (Ff), the signal attenuation is considerably lower than predicted by the Beer's law. Even at an OD = 20 ($\Delta z \approx 1600$ μm) the amplitude of the signal backscattered

by the reflecting interface remains high. A linear fit (least squares) through the experimental data leads to the attenuation constant $\alpha = 2.9\ \text{mm}^{-1}$. Thus, the attenuation constant $\alpha = 3.0\ \text{mm}^{-1}$ predicted by our model is in excellent agreement with experimental data. As shown in Fig. 4.9b, our theoretical value was obtained by a linear fit between three points.

With the confocal configuration (Cf), the linear fit through the experimental data yields $\alpha = 5.7\ \text{mm}^{-1}$, corresponding to an attenuation slightly lower than given by Beer's law ($\alpha = 6.2\ \text{mm}^{-1}$). The lower experimental coefficient is due to the detection of MSL residuals, in agreement with other studies [53, 54]. In addition, these results demonstrate the significant rejection of MSL obtained in point scanning OCT.

To further test our model and investigate the influence of the sample properties, we repeated the same experiment with a widely scattering solution ($g = 0.55$). In full-field configuration we obtained $\alpha = 6.1\ \text{mm}^{-1}$, that is, nearly no signal enhancement as compared with Beer's law predictions. Again, our model proves to be in excellent agreement with this value, since it predicted an attenuation constant $\alpha = 6.0\ \text{mm}^{-1}$. As shown in Fig. 4.9b, this theoretical value was obtained by a linear fit between three points. Since there is no significant deviation from Beer's law with the wide-angle scattering solution, we conclude that, in our case, only the forward-scattered light accounts for signal enhancement.

The significant deviation from Beer's law in FF-OCT for forward-scattered light reveals that the contribution of MSL relative to ballistic light dominates already at moderate probing depths. In the investigated case (Ff, $g = 0.93$), at a depth corresponding to one scattering mean free path ($\Delta z = 200\ \mu\text{m}$), the ballistic and MSL components of the OCT signal are approximately equivalent. In point-scanning OCT, MSL contribution typically dominates after several mean free paths [55]. Last but not least, the excellent agreement between the experimentally determined coefficients α and the theoretically predicted values reveal the propensity of our model to provide an accurate extrapolation of tissue properties from OCT measurements. This important application of OCT is the object of intensive research [53, 56, 57].

4.4.3 *Additional Results and Conclusions*

The dependence of cross talk noise on some important design parameters of the optical system was investigated in a previous study [11]. Both experimental and theoretical results were reported for full-field illumination diameters (D = 420 μm, 210 μm and 85 μm), numerical apertures of the sample objective (NA = 0.25, 0.1 and 0.05), as well as the source coherence length (l_c = 34 μm and 15 μm). Experimental and theoretical results were in very good agreement.

The above referred results and those presented in Section 4.4.1 led us to the conclusion that cross talk increases with the full-field diameter, numerical aperture, source coherence length and sample optical density, and strongly depends on sample anisotropy. Therefore, design guidelines for minimal cross talk contribution, would generally recommend reducing the full-field diameter, the numerical aperture and the source coherence length down to a value depending on the sample properties. When striving to reduce the numerical aperture, a trade-off between the highest transverse resolution and the lowest cross talk must be found. A broader source spectrum only marginally favors cross talk rejection. Another evidence of the strong cross talk contribution is provided by our observations of the significant deviation from Lambert–Beer's law, revealing that the transition from single scattering to diffuse light regime happens for much lower optical depths in FF-OCT than in point scanning OCT.

4.5 Cross Talk Suppression

The results presented in the previous section reveal to what extent cross talk-generated noise can limit FF-OCT. We will now experimentally investigate if the spatial coherence gating, introduced in Section 4.1.3, can be exploited for cross talk suppression. To prove our concept, we will investigate the cross talk rejection capability of spatial coherence gating by comparing spatially coherent to SII, under the same experimental conditions (setup and sample). We will show that rejection of cross talk by spatial coherence

gating is comparable to that achieved in point-scanning OCT. To further investigate rejection performance, we will compare confocal illumination with SII.

4.5.1 *Setup and Sample*

The optical setup (Fig. 4.10) consists of a Linnik interferometer with a flip mirror (FM) allowing selecting either spatially coherent or SII. In both configurations, the image of the sample is obtained by lenses L_4 and L_5 forming a $\times$ 30 magnifying microscope. The imaging optics and image construction method, which consists of a translation stage (TS) moving an optical fiber (OF) with appropriate core size, are the same as in our previous experimental setup. Except for the bandpass filter, which is increased to 1.4 kHz to account for the broader optical source bandwidth (see below), the same signal detection and processing (SDP) scheme, common to both configurations in Fig. 4.10, was employed in our previous experimental setup (see details in Section 4.3.1).

SCI is obtained with FM at 45° so as to select the interferometer source arm with the single mode fiber (SF). Details on the working principle of this configuration are provided in Section 4.3.1. Here the source is a mode-locked Ti:Sapphire laser (MLTS) whose spectrum is centered around 800 nm with a 70 nm bandwidth (FWHM).

SII is obtained with FM vertical so as to select the interferometer source arm with the multimode fiber (MF). The light from a 100 W Hg arc lamp injected (thermal light source) into MF allows delivering highly spatially incoherent light into the interferometer. The use of a multimode fiber provides a uniformly bright (equivalent to Koehler illumination) and easy to handle light source. In addition, the well-defined source size and geometry facilitate system design. In our case, the 550 μm fiber core, positioned at the focal plane of L_1, is directly imaged on the focal plane of objective L_4, leading to a 400 μm diameter full field.

In our design the sample objective aperture, which corresponds to the entrance pupil of the illumination system, is filled with spatially incoherent light. As explained in Section 4.3.1, the fulfillment of this requirement provides a design optimal for spatial coherence gating, that is, cross talk noise rejection capabilities.

Moreover, with a fiber NA of 0.21 and an objective NA of 0.25, the power throughput is nearly optimal since the spatial extent on the source side nearly corresponds to that on the sample side ($0.21^2 \times 550 \cong 0.25^2 \times 400$).

For a relevant comparison between spatially coherent and SII, full-field diameter, temporal coherence gating, and power must be the same in both configurations. The full-field intensity profile depends on the illumination. In SCI, a Gaussian beam is collimated onto the sample while, in SII, a top hat intensity profile is obtained by imaging the multimode fiber core. The waist (at 1/e) of the Gaussian illumination profile matches the 400 μm large incoherent full-field illumination (see Fig. 4.10, bottom inset). We attribute the relatively noisy top hat profile to insufficient polishing of our multimode fiber.

To obtain a similar spectrum with the mode-locked Ti:sapphire laser and the Hg light source, a smooth portion of the latter's spectrum—between 750 nm and 850 nm—is filtered through a combination of high- and low-pass interference filter (IF). As illustrated in the top inset of Fig. 4.10, very similar autocorrelation function envelopes are obtained for both sources. The corresponding measured longitudinal resolutions at FWHM in air are 4 and 4.5 μm, with the Hg and pulsed laser sources, respectively. The side lobes present in the filtered Hg source and in the mode-locked fs Ti:sapphire laser autocorrelation functions, are due to a nearly squared spectrum (resulting from the spectral filtering) and to polarization effects in the 100 meter long single mode fiber, respectively.

To illuminate the sample with the same power as with the Hg source, the mode-locked Ti:sapphire laser power was attenuated to 1 mW with a neutral density filter placed between L_2 and L_3.

The sample is a US air force reflecting resolution target covered with a scattering solution. The latter, consists of 2050 nm polystyrene microspheres diluted in de-ionized water, yielding an anisotropy parameter $g = 0.93$. A cell, with inner thickness of 650 μm, delimited by the resolution target and a 150 μm thick cover glass, was filled either with water or with the scattering solution. Full-field illumination was centered on element 2, group 6, of the resolution target (71.8 lines/mm) whose longitudinal position

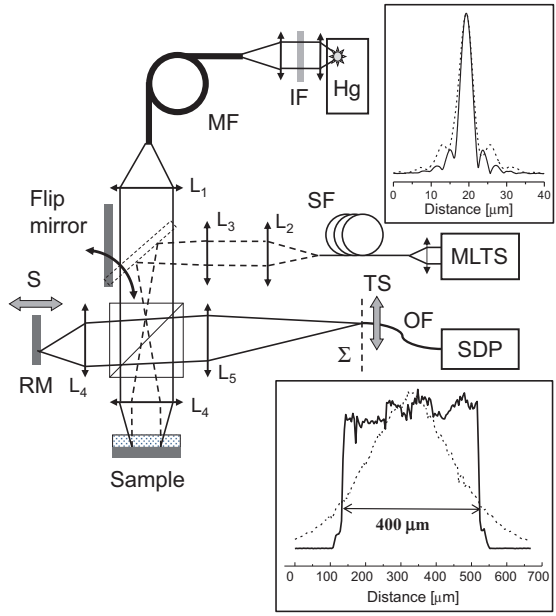

Figure 4.10 Scheme of an FF-OCT setup with spatially coherent (flip mirror at 45°) and spatially incoherent (flip mirror vertical) illumination: mercury arc lamp (Hg); mode-locked fs Ti:sapphire laser (MLTS); single-mode fiber (SF); multimode fiber (MF); interference filters (IF); reference mirror (RM); achromatic lenses (L_1, L_2, L_3, and L_5); microscope objectives $\times$ 10, NA = 0.25 (L_4); scanner (S); translation stage (TS); optical fiber (OF); signal detection and processing (SDP). Top inset: autocorrelation function envelopes measured in air for Hg (solid curve) and for MLTS (dashed curve) sources. Bottom inset: normalized full-field illumination profiles obtained with spatially coherent (dashed curve) and spatially incoherent illumination (solid curve).

was adjusted, with the cell filled with water, to form an image in the focal plane of L_5. Water was then replaced by the scattering solution whose scattering coefficient, measured independently with the method in Ref. [49], corresponds to 8 optical depths in the cell (two ways).

Note that, unlike for the half-mirror sample used for our quantitative investigation in Section 4.4, the glass interface between the reflecting stripes of the resolution target contributes to the OCT signal. This is not a problem in this comparative study.

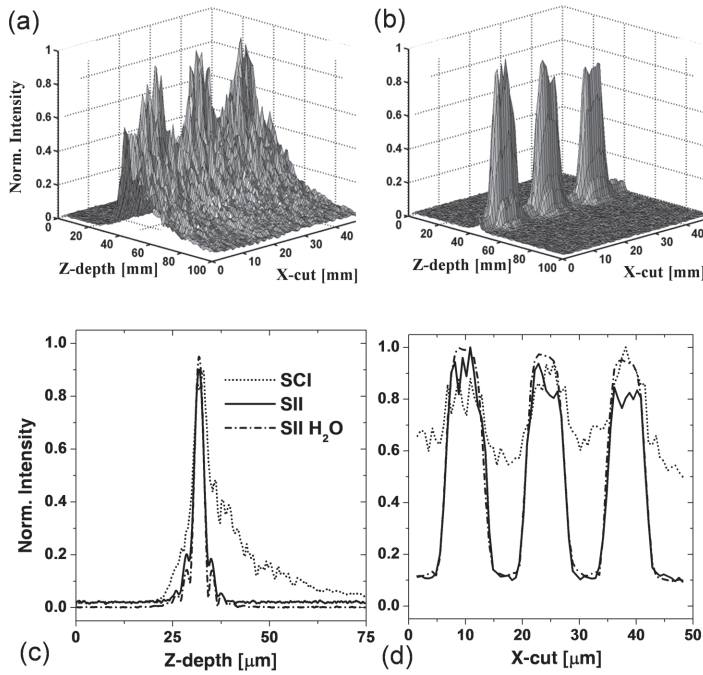

Figure 4.11 Cross-sectional FF-OCT image of a US Air Force resolution target covered with a scattering solution (OD $= 8, g = 0.93$): (a) spatially coherent illumination (SCI); (b) spatially incoherent illumination (SII); (c) cuts along the *z*axis of Fig. 4.2a (across the middle stripe), (d) cuts along the x axis of Fig. 4.2b (across the reflecting target interface). The curves labeled "SII H_2O" correspond to the same cuts of the same image acquired in water with SII. All curves are normalized and correspond to an average of 25 demodulated signals.

4.5.2 *Results*

Figures 4.11a and 4.11b show a three-dimensional representation of OCT cross-sectional images of the pattern's stripes—with the normalized intensity on the vertical axis—obtained with spatially coherent and SII, respectively. Despite short temporal coherence gating, SCI generates a considerable amount of cross talk noise, degrading both longitudinal and tranverse resolutions (Fig. 4.11a). The plots correspond to the average cross talk signal of 25 demodulated OCT signals (see Section 4.3.1). With full-field SII, the

spatial coherence gating provided by our optimal design strongly reduces cross talk noise, and in turn yields a good resolution of the three stripes (Fig. 4.11b).

For a quantitative estimate of spatial coherence gating efficiency, longitudinal cuts of the SCI and SII three-dimensional plots are compared. Cuts along the *z* axis (across the middle stripe), and those along the *x* axis (across the sample interface), are shown in Fig. 4.11c and Fig. 4.11d, respectively. It appears that the cross talk-generated noise is responsible for a loss of contrast and resolution, which can be restored with SII.

To further illustrate the spatial coherence gating efficiency, the same cross-sectional image was acquired in water with SII. The two normalized longitudinal cuts displayed in Fig. 4.11c and Fig. 4.11d correspond to plots obtained with SII in water (dash-dot curves) and in the scattering solution (solid curves). Except slightly higher amplitude side lobes and a more rippled profile in the scattering solution, their near identity reveals that in our case, longitudinal and tranverse resolutions are fully restored. The slight differences observed can be attributed to a noisy illumination intensity profile as well as to possible particle aggregates of the scattering solution at the resolution target interface.

For the same experimental setup, comparative results of spatially coherent with incoherent illumination for an ex vivo tooth have been reported [12]. SII has provided a more accurate image revealing new structures.

Comparison of confocal illumination with SII revealed that spatial coherence gating achieves cross talk suppression to the same extent as point-scanning OCT. As mentioned in Section 4.3.1, confocal configuration with properties equivalent to point-scanning OCT is achieved by simply removing lens L_3 in our setup (see Fig. 4.10). The monomode fiber is then imaged onto the sample providing a confocal spot illumination. The latter is attenuated with neutral density filters so as to obtain a sensitivity of 75 dB in both configurations. We use the full-mirror sample (see Section 4.3.2), with scattering solution with optical density OD $= 8$ and anisotropy $g = 0.85$. The correlograms obtained reveal that in both configurations cross talk rejection is equally efficient along the longitudinal dimension (Fig. 4.10). Differences near the side lobes are likely due to scanner instabilities as well as to residual MSL.

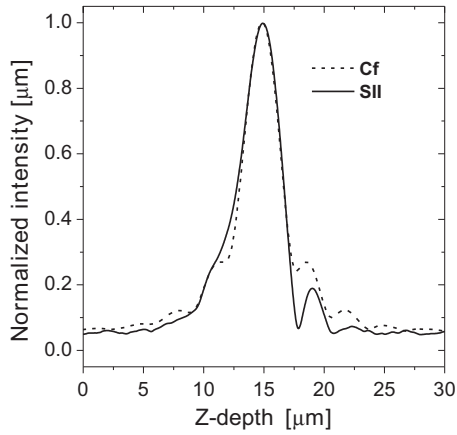

Figure 4.12 Comparison of FF-OCT with spatially incoherent illumination (SII) to point-scanning OCT with confocal configuration (Cf) for a mirror covered with the scattering solution (OD $= 8$, $g = 0.85$).

Our results demonstrate that cross talk noise generated in FF-OCT by SCI can be suppressed with SII provided by a thermal light source. With SII, the performance of FF-OCT is comparable to that of point-scanning OCT. However, despite the fact that FF-OCT requires less brightness than point-scanning OCT, the power per spatial mode radiated by thermal light sources is too low to permit a high SNR while maintaining a fast acquisition speed. This issue is discussed in the conclusions of this contribution.

We would like to emphasize that, besides allowing for spatial coherence gating, a thermal light source has a naturally broad spectrum, offering a very high longitudinal resolution at lower complexity and cost.

4.6 Conclusions and Discussions

4.6.1 *Full-Field OCT*

The theoretical and experimental investigations of FF-OCT presented in this chapter reveal the crucial role played by the nature of the light source. Despite temporal coherence gating, SCI generates

considerable optical cross talk noise, which prevents shot-noise-limited detection and diffraction-limited imaging in scattering samples.

Cross talk dependence on several important parameters of the optical system and on sample properties was investigated in a comprehensive study. The results have brought quantitative knowledge of cross talk noise contribution in FF-OCT relying on SCI, which has in turn allowed the elaboration of elementary design guidelines (see Section 4.4.3). The significant cross talk noise contribution drastically reduces the scope of practical applications in biological imaging. In principle, FF-OCT incorporating SCI is restricted to very moderately scattering samples. The method is suitable for topographic measurements.

By taking a closer look at the coherence properties of MSL in the context of OCT detection methods, we were able to explain how cross talk can be suppressed by exploiting spatially incoherent light. We have shown experimentally how SII realized with a thermal light source permits cross talk suppression, that is, rejection of MSL, to a level comparable to that of point-scanning OCT. This outstanding feature, combined with the naturally broad spectrum the thermal light source, allows the measurement of en face cross-sectional images with high quality and resolution, at minimum cost and complexity.

The main weakness of this method—as so far implemented—is its relatively low measurement speed, which does not allow observation of dynamic phenomena or in vivo imaging without artefacts due to sample motions. Thus, FF-OCT incorporating SII is incontestably a valuable method for obtaining high quality en face cross-sectional images, but remains mainly restricted to the observation of in vitro specimen.

The cause of limitation in measurement speed lies in (i) the insufficient performance of conventional detectors, and (ii) the relatively low brightness of thermal light sources. As reported in the introduction, the first limitation, of technological nature, can be overcome with presently available CMOS detectors endowed with custom functionality for OCT imaging (Heliotis AG). The second limitation, of fundamental nature, comes from the power per spatial mode radiated by thermal light sources that remains too weak to

allow a sufficient sensitivity while maintaining a fast acquisition speed.

To overcome this limitation, an extremely bright spatially incoherent light source is required. Increasing the temperature of a thermal light source above the 6000 K offered by arc lamps (e.g., with a plasma) is not trivial at all. An alternative might be the creation of a so-called pseudothermal light source [58] obtained by destroying the spatial coherence of a powerful broadband laser source, that is, by creating a speckle field with very low degree of correlation between the speckles. This can be achieved by generating fast random fluctuations, for instance, with a rotating diffusor [20] or dynamical mode mixing in a multimode fiber [59]. However, it is not trivial to generate fluctuations much shorter than the actual OCT measurement time per probe volume. This is a requirement for obtaining sufficient statistical averaging to get a low enough degree of correlation for cross talk suppression [20]. Alternatively, a recently investigated solution to create an uncorrelated speckle field relies on the injection of light from a broadband laser into a multimode fiber [21]. Setting up appropriate length and diameter of the fiber, delays exceeding the source temporal coherence time between modes propagating within the fiber can be generated so as to obtain a low degree of spatial coherence at the fiber exit. However, we believe that this method should be carefully investigated prior to implementation.[e] Thus, the creation of a pseudothermal light source suitable for FF-OCT does not seem trivial. A viable solution for creating a spatially incoherent light source might be an extended superluminescent light source based on the broadband fluorescence of a Ti:Al_2O_3 waveguide crystal [15].

Note that ANSI norms regarding the maximum exposure time of biological samples limit the increase of source power, which may in turn ultimately set a limitation to the method.

[e]The following two effects should be considered carefully. First, the intercoupling between modes propagating into the multimode fiber with different path lengths may alter the source autocorrelation function, causing problems such as deleterious harmonics. Second, the delays between modes are altered—and in the worst case fully compensated—by the random propagation of MSL in the sample. Should the worst case prevail, conditions for cross talk noise generation would be restored.

The en face image of biological structures obtained with FF-OCT is of particular interest since it may complement information provided by the longitudinal image obtained with FD-OCT [6, 18]. Moreover, the interpretation of en face views is often more familiar to specialists, such as ophthalmologists. A new generation of FF-OCT systems incorporating an ultrabright light source and a custom detector array may well compete with ultrafast FD-OCT systems (see introduction) regarding image acquisition speed. Should the sample be scanned in the longitudinal dimension or dynamical focusing be implemented [60, 61], the new generation of FF-OCT systems may also become a valuable alternative for ultrafast three-dimensional measurements. Actually, it may provide the most accurate three-dimensional measurements thanks to its inherently superior transverse resolution.

Alternatively, a very interesting modality for ultrafast three-dimensional measurements based on FD-OCT operation allows directly obtaining en face images thanks to a swept-laser source [59]. However, to achieve cross talk suppression, the spatial coherence of the swept-laser source beam must be destroyed so as to create a pseudothermal light source, what is not trivial as explained above.

It should not be forgotten that, since this new generation of fast measuring FF-OCT systems relies on unconventional detectors and sources, the access to measurement speeds permitting reliable in vivo measurements can only be gained at the expense of cost and simplicity, which are major attributes of the previous generation. However, like with the sophisticated femtosecond laser sources, novel detectors and sources for FF-OCT should become more commonplace.

4.6.2 *Modeling Multiple Scattering in OCT*

We have conducted a comprehensive study of multiple scattering effects in FF-OCT realized with SCI. The agreement between theoretical and experimental results for a wide range of different parameters was very good, confirming the validity of our model for MSL in OCT and, implicitly, the relatively simple assumptions on which it rests. Thus, the role of multiple scattering in OCT does not seem to be as complex as so far suggested by several studies

and models. Indeed, to the contrary of the widespread belief that a relevant OCT model should account for a partial correlation between interfering fields, we have explained why, in the context of OCT detection methods, multiple scattering actually induces neither a loss of spatial coherence of the sample field nor a reduction of the correlation between the latter and the reference field. This means that, for path length differences between the reference and sample arms falling within the source coherence length, the reference and sample fields interfere with a contrast determined uniquely by the source autocorrelation function. Multiple scattering generates a speckle noise contribution to the ideal OCT signal, but does not reduce the interference contrast.

Based on this important result, we have developed a comprehensive model of OCT where the signal is modeled as a sum of stationary random phasors and treated as a statistical signal. The mean intensity of this random signal, which is usually the variable of interest, can be calculated thanks to classical results of statistical optics and to a Monte Carlo simulation. This approach is very different from that of other models based on a Monte Carlo simulation, which take into account the effect of multiple scattering such as, for example, Ref. [62]. In the latter model the phase information, which depends on the history of scattering events, is recorded for each photon, represented by a plane wavelet. Thus, a simulation yields a sum of randomly delayed wavelets, which generate speckles. To obtain the mean signal, essentially the quantity of interest, many of such complicated and lengthy simulations must be run. In our model, the mean and the variance can be directly calculated thanks to the assumption that photons can undergo random phase excursions in the scattering medium of at least 2π.

The Monte Carlo simulation, necessary for the calculation of the raw spatiotemporal distribution of light, makes our model semianalytical. It is the prize one has to pay for accessing ranges where the diffusion approximation is not verified. Although our model is not as elegant as a fully analytical model, it offers the advantage of high versatility. Indeed, unlike fully analytical models, it is neither restricted to strongly simplified media nor limited by initial assumptions, such as the diffusion approximation or the small angle approximation.

As briefly discussed in Section 4.1.2.3, other existing models of OCT accounting for multiple scattering, are based on the extended Huygens–Fresnel principle and the use of mutual coherence functions MCFs [34, 35]. The calculation of MCFs relies on some spatial and temporal statistical averaging, generally yielding a reduction of correlation between the reference and sample fields. Thus, these models are incompatible with the two fundamental assumptions on which our model rests. Indeed, as emphasized in Section 4.1.2, statistical averaging is not applicable because of the high degree of spatial coherence of the measured sample field and of the short measurement time per probe volume. Therefore, our model implicitly puts in question other existing models accounting for multiple scattering in OCT. Interested readers can find a more thorough discussion of this topic in Ref. [33].

We do hope that our study and model will help to fully appreciate the role of multiple scattering in OCT and stimulate the research in this field. Future work of interest with our model could be a study of multiple scattering effects in point-scanning OCT in highly diffuse media such as skin. This would be particularly relevant for FD-OCT, in which confocal spatial filtering is inherently limited. Investigations of multiple scattering in OCT could be of particular interest when accounting for real tissues properties in the Monte Carlo simulation. Conclusions of our study may well concern a wider class of imaging methods limited by cross talk, such as parallel time-resolved detection [63], laser Doppler imaging [64] or holography with a broadband light source [65].

Appendix A: Independence of the Parameters u_j and L_j

The derivation of Eq. 4.18 requires assumption (ii) in Section 4.2.2. More specifically, this implies that u_j and L_j are independent, which is generally not the case. However, for our specific OCT case, it suffices to verify this condition only "locally," that is, for a relatively short path length interval ΔL in the order of the source coherence length l_c. Indeed, in the first approximation, the module of the source autocorrelation function $g_0(z)$ is null outside l_c. Thus, only the interval determined by l_c, needs to be considered. Independence

between u_j and L_j requires first that the depth of field set by the sample objective NA is larger than the longitudinal resolution set by the source coherence length, which is usually the case in OCT. Second, the interval $\Delta L \approx l_c$ must contain path lengths L_j having accumulated the same number of scattering events. Indeed, the field coefficients u_j also depend on the number of scattering events due to loss of energy in scattering and absorption. This second condition is more restrictive and needs to be discussed. With the anisotropy g, corresponding to the mean scattering angle cosine, $\Delta L \approx (1\text{–}g)\mu_S$, where μ_S is the sample scattering coefficient in inverse millimeters. Thus, the larger g and μ_S, the shorter is ΔL_j; that is, the more difficult it is to fulfill the condition $\Delta L_j \geq \Delta L \approx l_c$. For our preliminary experiment with $l_c = 15$ μm and sample scattering properties ($\mu_S = 1/\text{OD} = 1/8$, $g = 0.85$) yielding $\Delta L_j \approx 19$ μm, we have $\Delta L > l_c$. Since OCT is generally not applied to $\mu_S > 10\ \text{mm}^{-1}$ (skin properties), a large g is in principle more critical. However, with increasingly shorter coherence lengths in present day OCT systems, our second condition is generally satisfied.

Note also that, without absorption, our second condition can be significantly relaxed since backscattering losses are negligible; that is, the influence on the number of scattering events is negligible on u_j coefficients. Indeed, Mie functions reveal that for $g > 0.7$ (as met in most biological samples) nearly all light energy is scattered under $2\pi sr$ in the direction of the wave propagation.

Appendix B: Sum of a Deterministic and a Random Phasor

To model the practical case corresponding to our experiments (mirror embedded in a scattering solution), it is necessary to account for the deterministic phase of light reflected by the mirror without scattering events (see Section 4.2.2). To account for this ballistic contribution, a deterministic phasor sum with amplitude S is added to the random phasor sum of Eq. 4.14,

$$S(z) + Q(z)\exp\left(-i\Phi(z)\right) = u_0\left|g_0(z-L_0)\right|\exp\left(-ik_0L_0\right) + \sum_{j=1}^{N} u_j\left|g_0(z-L_j)\right|\exp\left(-ik_0L_j\right), \tag{4.22}$$

where L_0 is the sample mirror position. Adopting the convention $L_0 = 0$, the additional path lengths are defined relative to the sample mirror interface leading to $S(z) = u_0\, g_0(z)$.

The phasor amplitude described by Eq. 4.22 obeys a Rician probability density function, whose mean is given by [31]

$$\overline{A'(z)} = \sqrt{\frac{\pi}{2}}\sigma(z)\exp\left(-\frac{\beta^2(z)}{4}\right) \times \left[\left(1+\frac{\beta^2(z)}{2}\right) I_0\left(\frac{\beta^2(z)}{4}\right) + \frac{\beta^2(z)}{2} I_1\left(\frac{\beta^2(z)}{4}\right)\right], \tag{4.23}$$

where

$$\beta(z) = \frac{S(z)}{\sigma(z)} = \frac{u_0 g_0(z)}{\sigma(z)} \tag{4.24}$$

and where $\sigma(z)$ is the distribution's standard deviation. I_0 and I_1 are modified Bessel functions of the first kind with order zero and one, respectively. According to our analysis in Section 4.2.3, expressing the coefficient u_0 in $\beta(z)$ as a function of I_v for practical implementation of a Monte Carlo simulation yields

$$u_0 = \sqrt{U_0} = \sqrt{I_B}, \tag{4.25}$$

where I_B is the intensity of the ballistic light, determined either theoretically (Lambert–Beer's law) or by the Monte Carlo simulation.

Thus, the mean signal detected from a sample such as in our preliminary experiment, i.e the mean value of $i_D(z)$ in Eq. 4.13, is proportional to $\overline{A'(z)}$ and can be calculated by combining Eqs. 4.21 and 4.23–4.25. Note however that, even in the presence of a relatively large deterministic phasor, Eq. 4.21 may lead to an excellent approximation. Indeed, with the examples presented in Section 4.4, we obtained very similar results in nearly all cases, when using either Eq. 4.21 or the full treatment to account for the deterministic phasor.

References

1. Dunsby, C., and French, P. M. W. (2003). Techniques for depth-resolved imaging through turbid media including coherence-gated imaging. *J. Phys. D*, **36**, pp. R207–R227.

2. Rudolph, W., and Kempe, M. (1997). Topical review: trends in optical biomedical imaging. *J. Mod. Opt.*, **44**, pp. 1617–1642.
3. Fercher, A. F., Drexler, W., Hitzenberger, C. K., and Lasser, T. (2003). Optical coherence tomography: principles and applications. *Rep. Prog. Phys.*, **66**, pp. 239–303.
4. Izatt, J. A., Hee, M. R., Owen, G. M., Swanson, E. A., and Fujimoto, J. G. (1994). Optical coherence microscopy in scattering media. *Opt. Lett.*, **19**, pp. 590–592.
5. Kempe, M., Genack, A. Z., Rudolph, W., and Dorn, P. (1997). Ballistic and diffuse light detection in confocal and heterodyne imaging systems. *J. Opt. Soc. Am. A*, **14**, pp. 216–223.
6. Podoleanu, A. Gh., and Rosen, R. B. (2008). Combinations of techniques in imaging the retina with high resolution. *Prog. Retinal Eye Res.*, **27**, pp. 464–499.
7. Grajciar, B., Pircher, M., Fercher, A., and Leitgeb, R. (2005). Parallel Fourier domain optical coherence tomography for in vivo measurement of the human eye. *Opt. Express*, **13**, pp. 1131–1137.
8. Vabre, L., Dubois, A., and Boccara, A. C. (2002). Thermal full-field optical coherence tomography. *Opt. Lett.*, **27**, pp. 530–532.
9. Bourquin, S., Seitz, P., and Salathé, R. P. (2001). Optical coherence tomography based on two-dimensional smart detector array. *Opt. Lett.*, **26**, pp. 512–514.
10. Akiba, M., Chan, K. P., and Tanno, N. (2003). Full-field optical coherence tomography by two-dimensional heterodyne detection with a pair of CCD cameras. *Opt. Lett.*, **28**, pp. 816–819.
11. Karamata, B., Leutenegger, M., Lambelet, P., Laubscher, M., Bourquin, S., and Lasser, T. (2005). Multiple scattering in optical coherence tomography. Part II: experimental and theoretical investigation of cross talk in wide-field optical coherence tomography. *J. Opt. Soc. Am A*, **22**, pp. 1380–1388.
12. Karamata, B., Laubscher, M., Lambelet, P., Salathé, R. P., and Lasser,T. (2004). Spatially incoherent illumination as a mechanism for cross talk suppression in wide-field optical coherence tomography. *Opt. Lett.*, **29**, pp. 736–738.
13. Drexler, W., Morgner, U., Kärtner, F. X., Pitris, C., Boppart, S. A., Li, X. D., Ippen, E. P., and Fujimoto, J. G. (1999). In vivo ultrahigh-resolution optical coherence tomography. *Opt. Lett.*, **24**, pp. 1221–1223.
14. Potsaid, B., Gorczynska, I., Srinivasan, V. J., Chen, Y., Jiang, J., Cable, A., and Fujimoto, J. G. (2008). Ultrahigh speed Spectral/Fourier domain OCT

ophthalmic imaging at 70,000 to 312,500 axial scans per second. *Opt. Express*, **16**, pp. 15149–15169.

15. Sacchet, D., Brzezinski, M., Moreau, J., Georges, P., and Dubois, A. (2010). Motion artifact suppression in full-field optical coherence tomography. *Appl. Opt.*, **49**, pp. 1480–1488.
16. Beaurepaire, E., Boccara, A. C., Lebec, M., Blanchot, L., and Saint-Jalmes, H. (1998). Full-field optical coherence microscopy. *Opt. Lett.*, **23**, pp. 244–246.
17. Oh, W. Y., Bouma, B. E., Iftimia, N., Yun, S. H., Yelin, R., and Tearney, G. J. (2006). Ultrahigh-resolution full-field optical coherence microscopy using InGaAs camera. *Opt. Express*, **14**, pp. 726–735.
18. Dubois, A., Grieve, K., Moneron, G., Lecaque, R., Vabre, L., and Boccara, C. (2004). Ultrahigh-resolution full-field optical coherence tomography. *Appl. Opt.*, **43**, pp. 2874–2883.
19. Fercher, A. F., Hitzenberger, C. K., Sticker, M., Moreno-Barriuso, E., Leitgeb, R., Drexler, W., and Sattmann, H. (2000). A thermal light source technique for optical coherence tomography. *Opt. Commun.*, **185**, pp. 57–64.
20. Karamata, B. (2004). *Multiple scattering in wide-field optical coherence tomography*, Ph.D. thesis EPFL **3001** (École Polytechnique Fédérale de Lausanne, Switzerland).
21. Dhalla, A. H., Migacz, J. V., and Izatt, J. A. (2010). Crosstalk rejection in parallel optical coherence tomography using spatially incoherent illumination with partially coherent sources. *Opt. Lett.*, **35**, pp. 2305–2307.
22. Laubscher, M., Ducros, M., Karamata, B., Lasser, T., and Salathe, R. (2002). Video-rate three-dimensional optical coherence tomography. *Opt. Express*, **10**, pp. 429–435.
23. Bordenave, E., Abraham, E., Jonusauskas, G., Tsurumachi, N., Oberl, J., Rullière, C., Minot, P. E., Lassègues, M., and Surlève Bazeille, J. E. (2002). Wide-field optical coherence tomography: imaging of biological tissues. *Appl. Opt.*, **41**, pp. 2059–2064.
24. Miller, D. T., Qu, J., Jonnal, R. S., and Thorn, K. (2003). Coherence gating and adaptive optics in the eye. *Proc. SPIE*, **4956**, pp. 65–72.
25. Lambelet, P. (2011). Parallel optical coherence tomography (pOCT) for industrial 3D inspection. *Proc. SPIE*, **8082**, p. 80820X.
26. Sinclair, L. C., Cossel, K. C., Coffey, T., Ye, J., and Cornell, E. A. (2011). Frequency comb velocity-modulation spectroscopy. *Phys. Rev. Lett.*, **107**, p. 093002.

27. Leitgeb, R., Hitzenberger, C. K., and Fercher, A. F. (2003). Performance of fourier domain vs. time domain optical coherence tomography. *Opt. Express*, **11**, pp. 889–894.
28. Yura, H. T. (1979). Signal-to-noise ratio of heterodyne lidar signal systems in the presence of atmospheric turbulence. *Opt. Acta*, **26**, pp. 627–644.
29. Karamata, B., Hassler, K., Laubscher, M., and Lasser, T. (2005). Speckle statistics in optical coherence tomography. *J. Opt. Soc. Am. A*, **22**, pp. 593–596.
30. Schmitt, J. M., Xiang, S. H., and Yung, K. M. (1999). Speckle in optical coherence tomography. *J. Biomed. Opt.*, **4**, pp. 95–105.
31. Goodman, J. W. (1985). *Statistical Optics* (Wiley Classics Library), pp. 44–45.
32. Yang, C., An, K., Perelman, L. T., Dasari, R. R., and Feld, M. S. (1999). Spatial coherence of forward-scattered light in a turbid medium. *J. Opt. Soc. Am. A*, **16**, pp. 866–871.
33. Karamata, B., Lambelet, P., Laubscher, M., Leutenegger, M., Bourquin, S., and Lasser, T. (2005). Multiple scattering in optical coherence tomography. Part I: investigation and modeling. *J. Opt. Soc. Am. A*, **22**, pp. 1369–1379.
34. Schmitt, J. M., and Knuettel, A. (1997). Model of optical coherence tomography of heterogeneous tissue. *J. Opt. Soc. Am. A*, **14**, pp. 1231–1242.
35. Thrane, L., Yura, H. T., and Andersen, P. E. (2000). Analysis of optical coherence tomography systems based on the extended Huygens-Fresnel principle. *J. Opt. Soc. Am. A*, **17**, pp. 484–490.
36. Mandel, L., and Wolf, E. (1995). *Optical Coherence and Quantum Optics* (Cambridge University Press, UK).
37. Davidson, M., Kaufman, K., Mazor, I., and Cohen, F. (1987). An application of interference microscopy to integrated circuit inspection and metrology. *Proc. SPIE*, **775**, pp. 233–341.
38. Lee, B. S., and Strand, T. C. (1990). Profilometry with a coherence scanning microscope. *Appl. Opt.*, **29**, pp. 3784–3788.
39. Somekh, M. G., See, C. W., and Goh, J. (2000). Wide field amplitude and phase confocal microscope with speckle illumination. *Opt. Commun.*, **174**, pp. 75–80.
40. Sun, P. C., and Leith, E. N. (1994). Broad-source image plane holography as a confocal imaging process. *Appl. Opt.*, **33**, pp. 597–602.

41. Ishimaru, A., Kuga, Y., Cheung, R., and Shimizu, K. (1978). Diffusion of a pulse in densely distributed scatterers. *J. Opt. Soc. Am. A*, **68**, pp. 1045–1050.
42. Patterson, M. S., Chance, B., and Wilson, B. C. (1989). Time resolved reflectance and transmittance for the non-invasive measurement of tissue optical properties. *Appl. Opt.*, **28**, pp. 2331–2336.
43. Ishimaru, A., Kuga, Y., Cheung, R., and Shimizu, K. (1983). Scattering and diffusion of a beam wave in randomly distributed scatterers. *J. Opt. Soc. Am. A*, **73**, pp. 131–136.
44. Jacques, S. L. (1989). Time resolved propagation of ultrashort laser pulses within turbid tissues. *Appl. Opt.*, **28**, pp. 2223–2229.
45. Pan, Y., Birngruber, R., Rosperich, J., and Engelhardt, R. (1995). Low-coherence optical tomography in turbid tissue: theoretical analysis. *Appl. Opt.*, **34**, pp. 6564–6574.
46. Smithies, D. J., Lindmo, T., Chen, Z., Nelson, J. S., and Milner, T. E. (1998). Signal attenuation and localization in optical coherence tomography studied by Monte Carlo simulation. *Phys. Med. Biol.*, **43**, pp. 3025–3044.
47. Yao, G., and Wang, L. V. (1999). Monte Carlo simulation of an optical coherence tomography signal in homogeneous turbid media. *Phys. Med. Biol.*, **44**, pp. 2307–2320.
48. Schmitt, J. M., and Kumar, G. (1996). Turbulent nature of refractive index variations in biological tissues. *Opt. Lett.*, **16**, pp. 1310–1312.
49. Van Staveren, H. J., Moes, C. J., van Marle, M. J., Prahl, S. A., and van Gemert, M. J. C. (1991). Light scattering in Intralipid-10% in the wavelength range of 400-1100 nm. *Appl. Opt.*, **30**, pp. 4507–4514.
50. Bohren, C. F., and Huffman, D. R. (1983). *Absorption and Scattering of Light by Small Particles* (Wiley-Interscience), p. 72.
51. Wang, L. H., Jacques, S. L., and Zheng, L.-Q. (1995). MCML: Monte Carlo modeling of photon transport in multi-layered tissues. *Comput. Methods Prog. Biomed.*, **47**, pp. 131–146.
52. Cheong, W. F., Prahl, S. A., and Welsh, A. J. (1990). A review of the optical properties of biological tissues. *J. Quantum. El.*, **26**, pp. 2166–2185.
53. Schmitt, J. M., Knuettel, A., and Bonner, R. F. (1994). Measurement of optical properties of biological samples in low-coherence reflectometry. *Appl. Opt.*, **32**, pp. 6032–6042.
54. Yadlowsky, M. J., Schmitt, J. M., and Bonner, R. F. (1995). Multiple scattering in optical coherence microscopy. *Appl. Opt.*, **34**, pp. 5699–5707.

55. Bizheva, K. K., Siegel, A. M., and Boas, D. A. (1998). Path-length-resolved dynamic light scattering in highly scattering random media: the transition to diffusing wave spectroscopy. *Phys. Rev. E*, **58**, pp. 7664–7667.
56. Faber, D. J., van der Meer, F. J., Aalders, M. C., and van Leeuwen, T. G. (2004). Quantitative measurement of attenuation coefficients of weakly scattering media using optical coherence tomography. *Opt. Express*, **12**, pp. 4353–4365.
57. Levitz, D., Thrane, L., Frosz, M. H., and Andersen, P. E. (2004). Determination of optical scattering properties of highly scattering media in optical coherence tomography. *Opt. Express*, **12**, pp. 249–259.
58. Martienssen, W., and Spiller, E. (1964). Coherence and fluctuations in light beams. *Am. J. Phys.*, **32**, p. 919.
59. Považay, B., Unterhuber, A., Hermann, B., Sattmann, H., Arthaber, H., and Drexler, W. (2006). Full-field time-encoded frequency-domain optical coherence tomography. *Opt. Express*, **14**, pp. 7661–7669.
60. Lexer, F., Hitzenberger, C. K., Drexler, W., Molebny, S., Sattmann, H., Sticker, M., and Fercher, A. F. (1999). Dynamic coherent focus OCT with dept-independent transversal resolution. *J. Mod. Opt.*, **46**, pp. 541–553.
61. Botcherby, E. J., Juskaitis, R., Booth, M. J., and Wilson, T. (2007). Aberration-free optical refocusing in high numerical aperture microscopy. *Opt. Lett.*, **32**, pp. 2007–2009.
62. Lu, Q., Gan, X., Gu, M., and Luo, Q. (2004). Monte Carlo modeling of optical tomography imaging through turbid media. *Appl. Opt.*, **43**, pp. 1628–1636.
63. Hebden, J. C., Kruger, R. A., and Song, K. S. (1991). Time resolved imaging through a highly scattering medium. *Appl. Opt.*, **30**, pp. 788–794.
64. Leutenegger, M., Martin-Williams, E., Harbi, P., Thacher, T., Raffoul, W., André, M., Lopez, A., Lasser, P., and Lasser, T. (2011). Real-time full field laser Doppler imaging. *Biomed. Opt. Express*, **2**, pp. 1470–1477.
65. Leith, E., Chen, H., Chen, Y., Dilworth, D., Lopez, J., Masri, R., Rudd, J., and Valdmanis, J. (1991). Electronic holography and speckle methods for imaging through tissue using femtosecond gated pulses. *Appl. Opt.*, **30**, pp. 4204–4210.